Geophysical Journal International

Geophys. J. Int. (2020) **223,** 543–560
Advance Access publication 2020 June 23
GJI Seismology

doi: 10.1093/gji/ggaa309

Bulk, shear and scattering attenuation beneath Hawaiian Volcanos and in the oceanic crust extending to the Aloha Cabled Observatory

Rhett Butler

Hawai'i Institute for Geophysics and Planetology, University of Hawai'i at Manoa, Honolulu, HI 96822, USA. *E-mail:* rgb@hawaii.edu

Accepted 2020 June 18. Received 2020 June 16; in original form 2020 January 31

SUMMARY

Seismic attenuation is measured from a swarm of 50 earthquakes in Kīlauea volcano in 2018, associated with caldera collapse. The traverse extends at nearly constant azimuth to the saddle between Mauna Loa and Mauna Kea, continuing to Maui beneath the distal flanks of three dormant volcanos. From Maui the traverse then extends seaward to the Aloha Cabled Observatory (ACO) on the seafloor north of O'ahu. The effective attenuation is measured with respect to an ω^{-2} earthquake source model. Frequency dependent Q_P and Q_S are derived. The initial path is shallow and uphill, the path to Maui propagates at mid-crustal depths, and the path to ACO extends through oceanic crust. The observations of $Q_P \leq Q_S$ over each traverse are modelled as bulk attenuation Q_K. Several attenuation processes are observed, including Q_μ, Q_K, $Q \sim f$, constant Q and scattering. The observation of bulk attenuation is ascribed to contrasting physical properties between basalt and water saturated vesicles. The ratio of Q values between shallow and mid-crustal propagation is used to derive an activation energy E^* for the undetermined shear attenuation mechanism. A Debye relaxation peak is fit to the $Q_S(f)$ and $Q_K(f)$ observed for the mid-crustal pathway. A prior high-frequency attenuation study near Wake Island compares well with this Hawaiian Q data set, which in general shows lower values of Q than observed for Wake.

Key words: Body waves; Seismic attenuation; Volcano seismology; Crustal structure.

1 INTRODUCTION

The Hawaiian Islands are among the most prominent geophysical features on Earth. The islands have risen from the seafloor to effective heights exceeding Mt Everest. The Island of Hawai'i has two of the most active volcanos globally, and their neighboring volcanoes are mostly dormant. Seismicity associated with the volcanism and the weight of the volcanos on the Pacific lithosphere extends ~400 km to O'ahu. The seismic hazard and earthquake occurrence rates in Hawaii are locally as high as that near the most hazardous faults elsewhere in the United States (Klein *et al.* 2001). Hawai'i sits upon a 'hot spot' or 'mantle plume' which may extend downward to the core–mantle boundary (Wilson 1963; Morgan 1971, 1972; Anderson 1975; Anderson & Natland 2005). As the Pacific lithosphere moves forward, this center of volcanism leaves a vestigial tracing of volcanos in its wake, out to Midway Island and then northward. The ramifications of heating and volcanism from the plume are to alter the crustal and lithospheric, thermal and seismic structure beneath the islands (e.g. Davies 1994).

In this study I have analysed seismic data to measure the effective Q for seismic wave propagation originating at a swarm of 50 earthquakes (M_w 5.2–5.4) which occurred during the 2018 collapse of the Kīlauea caldera (Neal *et al.* 2019). This study complements prior studies of these earthquake sources (Butler 2019) and their foreshocks (Butler 2020). Measuring both Q_P and Q_S I have identified where their ratio indicates a significant contribution from bulk attenuation Q_K, in addition to shear attenuation, Q_μ (Butler *et al.* 1987). Prior attenuation models for Hawai'i are reviewed. The effect of $Q_{\text{scattering}}$ on $Q_{\text{intrinsic}}$ is estimated and compared with results from Chouet (1976) and Mayeda *et al.* (1992). In principle, since many attenuation mechanisms are thermal (T) and pressure (P) activated processes, $Q = Q_0 \mathrm{e}^{-(E^* + P\bar{V})/RT}$ (Anderson 1967)—where E^* and $\bar{V}$ are an activation energy and volume and R is the universal gas constant—I have estimated the basalt activation energy from the ratio of shallow and mid-crustal Q_S, pressure and temperature from Hawai'i boreholes. Assuming the relaxation model for a standard linear solid, a simple Debye peak is fit to the variation of attenuation with frequency.

2 DATA SET

2.1 Propagation paths

The propagation paths for the study are shown in Fig. 1. The paths traverse beneath the Hawaiian volcanos: Kīlauea, Mauna Loa,

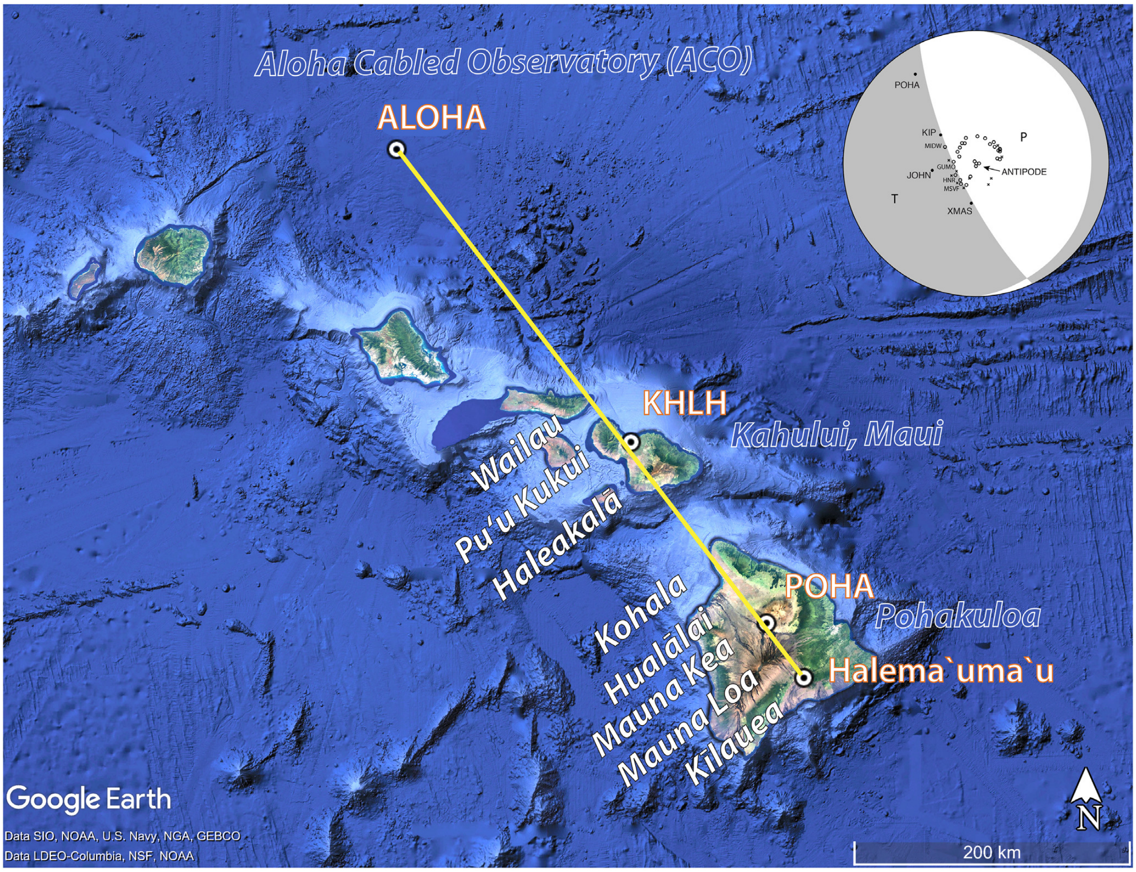

Figure 1. Map of the Hawaiian Islands and study area. The yellow line shows the propagation path from Halemaʻumaʻu crater in Kīlauea caldera to Pohakuloa (POHA), Kahului Maui (KHLH); and the Aloha Cabled Observatory (ALOHA). POHA is located on the saddle at 1990 m elevation. KHLH is located at 14 m. ALOHA is on the sea floor at 4728 m depth. Hawaiian volcanos whose distil flanks are traversed in propagation are highlighted left of the propagation line. The inset shows the composite focal mechanism of the 50 nearly identical earthquakes (Butler 2019).

Mauna Kea, Hualālai, Kohala, Haleakelā, Puʻu Kukui (West Maui) and Wailau (East Molokaʻi). The 50 earthquakes between May 29 and August 2 occurred within a 1.5-km radius at about 0.3 km median depth (for a list of events and map of their locations see table 1 and figure 1 in Butler 2019). As evident in Fig. 1, the paths share a common azimuth from the source, and thereby share mutual azimuthal source effects. The inset shows the composite focal mechanism of the 50 earthquakes from Butler (2019), where a detailed discussion of the events may be found. As the Kīlauea summit (Halemaʻumaʻu Crater) is at about 1600 m and the USGS reviewed hypocentres range from 1.4 to −1 km, the events nominally occurred near sea level.

The first path segment is to Global Seismographic Network (GSN, Butler *et al.* 2004) station POHA, Pohakuloa near the saddle of Hawaiʻi between Mauna Loa and Mauna Kea volcanos at an elevation of 1990 m. From the earthquake sources below Kīlauea summit near sea level, the shallow path to POHA is about 2–3 km 'uphill,' and measures the attenuation within the uppermost kilometres of Kīlauea and Mauna Loa to the edge of Mauna Kea. The mean of *P*- and *S*-wave group arrivals travel at about 4.5 and 2.8 $\mathrm{km\,s^{-1}}$, respectively.

The second segment extends from POHA to the Pacific Tsunami Warning Center (PTWC) seismic station KHLH, Kahului, Maui. The path to KHLH on Maui is deeper, extending from beneath Kīlauea caldera to the distal flanks of Mauna Loa, Mauna Kea, Hualālai, Kohala and Haleakalā to KHLH on Maui. Applying the Hawaiian Volcano Observatory (HVO) velocity structure for Hawaiʻi the mean *P*- and *S*-wave arrivals at KHLH have ray parameters of 1/6.8 and 1/4.1 $\mathrm{s\ km^{-1}}$, respectively. These *P*- and *S*-wave velocities correspond to mid-crustal velocities, ∼7 km deep.

The path to ALOHA extends the path from KHLH—including the distal edges of Puʻu Kukui and Wailau—and thence into the Pacific oceanic crust and lithosphere at the Aloha Cabled Observatory (ACO), which resides on the seafloor at 4728 m depth, about 110 km north of Oʻahu. Applying the Watts & ten Brink (1989) oceanic crust appropriate for the upward path from Maui to ACO, the mean *P*- and *S*-wave arrivals at ALOHA have ray parameters of 1/6.8 and 1/4.7 $\mathrm{s\ km^{-1}}$, respectively. Again, these *P*- and *S*-wave velocities correspond to mid-crustal velocities, ∼7 km deep.

2.2 Sensors and distance ranges

The primary sensor used for POHA is the Streckeisen STS-2 high-gain sampled at 100 samples per second (sps). The HHZ channel is triggered, but actively recorded all of the events at a distance of about ∼46 km. At KHLH the primary sensor is the STS-2 sampled continuously at 100 sps from the HHZ channel. KHLH is about 204 km from Halemaʻumaʻu. At the ACO the primary sensor is the ALOHA hydrophone, at 465 km distance from Halemaʻumaʻu. The ALOHA sensor recorded at 96 kHz is decimated to 400 Hz for initial review of frequency content, but then decimated to 100 Hz for compatibility with the KHLH and POHA data. The ALOHA sensor has been calibrated to a Paroscientific nano-resolution Digiquartz pressure gauge in the overlapping frequency band 1–10 Hz.

3 METHODOLOGY

In deriving the effective Q for the propagation paths, I adopted the basic methodology used by prior Hawai‘i studies (Scherbaum & Wyss 1990; Hansen *et al.* 2004; Lin *et al.* 2015) wherein the earthquake source displacement spectra decays as f^{-2} (i.e. Brune 1970; and Kaneko & Shearer 2014) beyond a measured corner frequency, f_c. In deriving the effective $Q(f)$, no presumption was made regarding the frequency dependence of Q.

The STS-2 and hydrophone data are converted into far-field displacement, $u(x,t)$, from which the amplitude spectrum $A(f)$ is derived. Initiating with the P- and S-wave arrival times, the data are sampled in 5.12 s windows, which also contain the energy maxima. To confirm appropriateness of window selection, a comparison with the Kanto district of Japan (Sato *et al.* 2012, fig. 8.10) found that 2–16 Hz S waves at 80–300 km distance show time offsets of predominantly 1–3 s between the S arrival and S maximum, the broadening attributed to scattering. Fig. 2 displays spectrograms showing the time–frequency content of the earthquake signals. The measurement of S-wave pulse broadening for this Hawaiian data set is impeded by the intense foreshock activity preceding the major events (Butler 2020). The spectral analysis of the P and S windows used the multitaper method (Park *et al.* 1987).

The earthquake spectrum $u(f)$ is modelled following Kaneko & Shearer (2014),

$$u\,(f) = \frac{\Omega_0}{1+(f/f_c)^2}, \tag{1}$$

where Ω_0 is the long-period spectral amplitude proportional to seismic moment, M_0 and the spectral fall-off of the source is proportional to f^{-2}. Ω_0 includes frequency independent effects such as geometric spreading, source radiation and site impedance.

The effective attenuation is expressed as ${}_{\mathrm{eff}}Q$, which is the ratio of the Imaginary to Real part of the complex modulus (shear μ or bulk K), whose functional form is $\mathrm{e}^{-\pi f x/Qc}$, where x is distance in km and c is the wave velocity (km s^{-1}). The amplitude spectrum is modelled as the product of the source with the effective attenuation,

$$A\,(x,f) = u\,(f)\;\mathrm{e}^{\frac{-\pi f x}{Qc}}. \tag{2}$$

Expressed in terms of $t^* = t/Q$ (e.g. van IJsseldijk *et al.* 2019) the exponent $\frac{-\pi f x}{Qc}$ is equivalent to $-\pi f t^*$. Solving for $Q(f > f_c)$,

$${}_{\mathrm{eff}}Q\,(f) \;=\; \frac{\pi f x}{\mathrm{c}\,[\log u\,(f) - \log A\,(f)]}\;. \tag{3}$$

In practice, both Q and effective Q are used interchangeably, but the basic model assumptions are still implicit. No attempt was made to correct for frequency dependent wave propagation effects using empirical Green’s function methods (e.g. Shearer *et al.* 2006) for several reasons: (1) the closest sensor at POHA did not reliably trigger on smaller magnitude events, (2) the more distant sites did not reliably have good signal-to-noise ratio (SNR), that is $A(f)_{\mathrm{SNR}} > 4$ and (3) the high background noise level from small events outside of the Kīlauea caldera. Nonetheless, the empirical Green’s function corrections used by Shearer *et al.* (2006) are <10 per cent. Similarly, no local site corrections are made for POHA and KHLH located on Hawaiian vesicular basalts, since the effective Q is derived from the signal fall-off with frequency in relation to the ω^{-2} earthquake source model.

3.1 *P* and *S* corner frequencies and spectra

An example of the amplitude spectral measurements for POHA is shown in Fig. 3. Only data with a SNR > 4 are used. The P and S corner frequencies f_c of the fifty earthquakes are determined from the closest station, POHA, by extrapolating the signal trend to the low-frequency amplitude maxima that is proportional to the seismic moment. These f_c are then averaged for P and S, respectively, ± the standard error of the mean: $f_c^P = 0.44 \pm 0.02$ and $f_c^S = 0.41 \pm 0.02$. The same f_c^P and f_c^S are used for POHA, KHLH and ALOHA. Although the log–log, linear trend of the signal is measured, effective ${}_{\mathrm{eff}}Q$ values are determined by (3) for each signal frequency from the log difference of the signal from the f^{-2} source.

3.2 Effective *Q*

From the P and S waves, Q_P and Q_S are, respectively, determined. Shear waves attenuate due to a complex shear modulus, μ, where the shear wave velocity $V_S = \sqrt{\frac{\mu}{\rho}}$, ρ is density and $Q_S \equiv Q_\mu$. Compressional waves experience losses both in shear (μ) and incompressibility (K) moduli, where $V_P = \sqrt{\frac{K+4\mu/3}{\rho}}$. The relationship between Q_P, Q_μ and Q_K is (Anderson 1989):

$$\begin{aligned} Q_p^{-1} &= L\,Q_\mu^{-1} + (1-L)\,Q_K^{-1} \\ L &= (4/3)(V_s/V_p)^2 \end{aligned} \tag{4}$$

For a Poisson solid exhibiting all attenuation in shear, $Q_P = \frac{9}{4}Q_S$ (e.g. Anderson & Given 1982). Therefore, where $Q_P < \frac{9}{4}Q_S$ then Q_K may be defined. Surprisingly, this condition is often met, and therefore Q_P, Q_S and Q_K are determined where applicable. Both Q_μ and Q_K measure the intrinsic anelasticity. Nonetheless, the relative contribution of elastic scattering of shear and compressional waves on intrinsic Q are considered in terms of $Q_{\mathrm{scattering}}$.

The paths to POHA and KHLH transit within the volcano edifices. The path to ALOHA extends from the 204 km path to KHLH and transits the oceanic crust. The attenuation observed at ALOHA also contains the attenuation observed at KHLH. To resolve the ${}_{\mathrm{eff}}Q$ for the path KHLH⟶ALOHA, consider the accumulative $t*$ (e.g. Cormier 1982):

$$t* = \int_{\mathrm{path}} \frac{\mathrm{d}t}{Q} \approx \sum\nolimits_i \frac{\Delta t_i}{Q_i} \tag{5}$$

The $t*$ for the whole path is the cumulative $t*$ for the path segments, where Δt_i is the path segment traveltime.

$$\begin{aligned} &t^*_{KHLH} + t^*_{\mathrm{KHLH}\rightarrow\mathrm{ALOHA}} = t^*_{\mathrm{ALOHA}} \\ &t^*_{\mathrm{KHLH}\rightarrow\mathrm{ALOHA}} = t^*_{\mathrm{ALOHA}} - t^*_{\mathrm{KHLA}}. \end{aligned} \tag{6}$$

Solving for Q over the path KHLH⟶ALOHA, we derive $Q_{\mathrm{KHLH}\longrightarrow\mathrm{ALOHA}}$ from measured values at KHLH and ALOHA.

$$\frac{\Delta t_{\mathrm{ALOHA}} - \Delta t_{\mathrm{KHLH}}}{Q_{\mathrm{KHLH}\rightarrow\mathrm{ALOHA}}} = \frac{\delta t_{\mathrm{ALOHA}}}{Q_{\mathrm{ALOHA}}} - \frac{\Delta t_{\mathrm{KHLH}}}{Q_{\mathrm{KHLH}}}. \tag{7}$$

The ${}_{\mathrm{eff}}Q$ for the path segment is calculated for each frequency where Q has been determined at both the beginning and end of a segment. For example, Q_S (and similarly for Q_P) over the KHLH⟶ALOHA segment requires Q_S^{KHLH}, measured at the same frequencies from the same earthquake. Moreover, Q_K requires both measured Q_P and Q_S at the same frequencies and for the same earthquakes. As a consequence, segmental Q measures are limited by the smallest frequency range of the elemental components contributing to a Q segment.

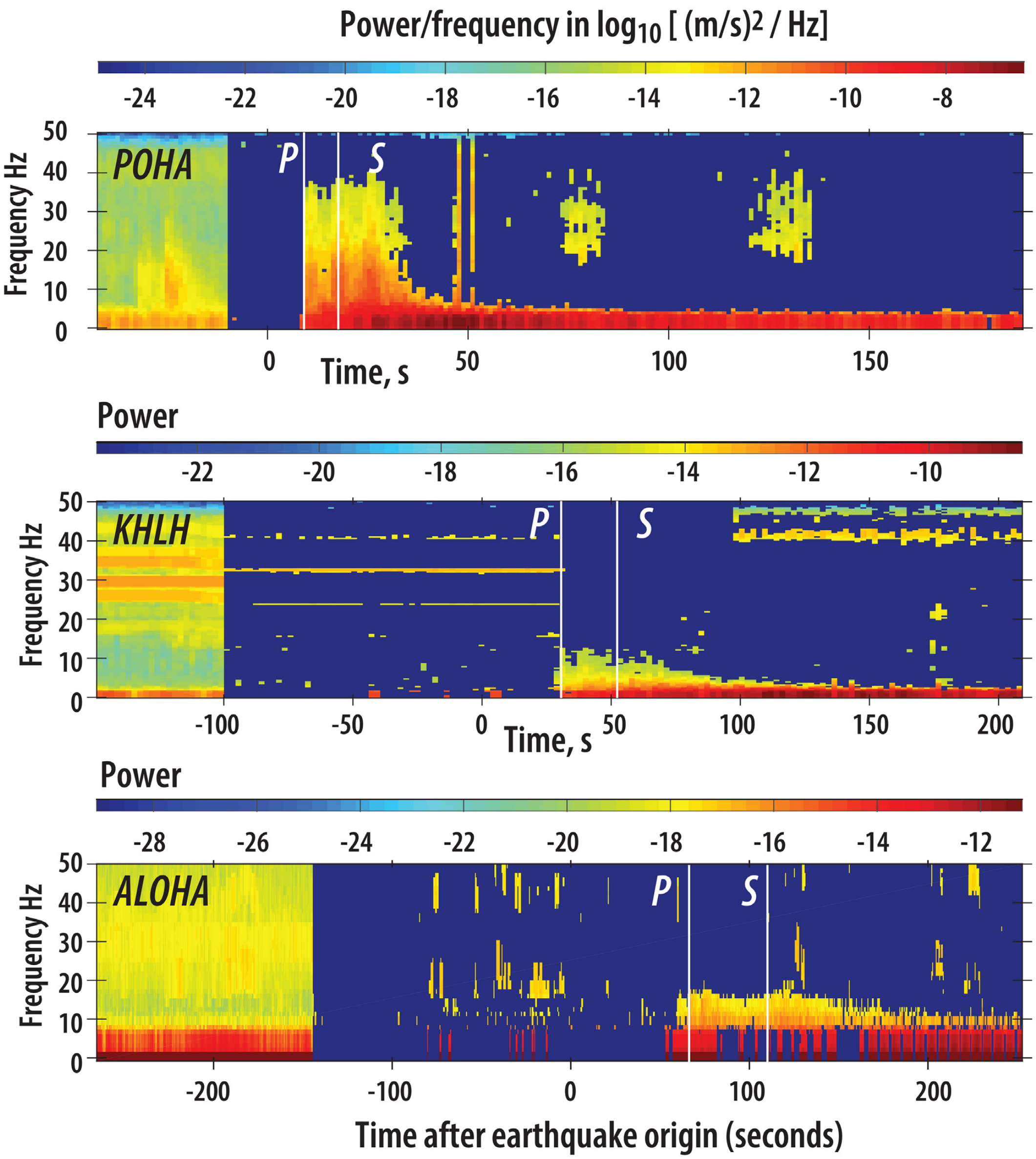

Figure 2. Spectrograms for POHA Pohakuloa (upper panel), KHLH Kahului (middle panel) and ALOHA, ACO (lower panel) are shown for the Halema‘uma‘u earthquake on 20-Jun-2018 14:22:23. Left portion of each panel displays the pre-event noise sample. To the right of the pre-event noise sample, only signals with a signal-to-noise ratio (SNR) ≥4 are plotted. The deep blue background indicates SNR < 4. Hence, the right portion displays the earthquake where SNR ≥ 4. Nominal *P* and *S* times are indicated. POHA and KHLH are sampled at 100 sps, whereas ALOHA is down-sampled from 96k to 100 sps The colour bars above each panel indicate the $\log_{10}$ power in each time–frequency interval. The *y*-axis is frequency Hz, whereas the time axis is in seconds with respect to the earthquake origin time.

For each frequency measurement, only data with a SNR > 4 are used. In each frequency band the *Q* values are determined for each earthquake. The joined results are then subjected to a median filter. The median absolute difference was applied to determine the 25 and 75 per cent percentiles, which encompass 50 per cent of the data in a given frequency band.

4 HAWAI‘I ATTENUATION LITERATURE REVIEW

Prior studies of attenuation on the Island of Hawai‘i are summarized in Fig. 4. The study Mayeda *et al.* (1992) built upon prior work by Aki & Chouet (1975), Chouet (1976) and Aki () using *S*-wave coda to derive both intrinsic and scattering *Q* through the relation $1/Q_{\mathrm{coda}} = 1/Q_{\mathrm{intrinsic}} + 1/Q_{\mathrm{scattering}}$. Frankel & Wennerberg (1987) note that in the approach developed by Aki (1980), the single-scattering model does not separate the intrinsic and scattering *Q* in its analysis of coda decay. It combines the two types of attenuation into a term called the ‘coda *Q*,’ which is determined from the decay rate of the coda. The single-scattering model assumes that the coda *Q* is equivalent to the *Q* of direct waves propagating through the medium. Mayeda *et al.* (1992) extended Aki’s method, but was unable fit the data in a self-consistent fashion. Nonetheless, the results of Chouet (1976) and Mayeda *et al.* (1992) suggest a frequency dependent Q_S, as well as $Q_{\mathrm{intrinsic}} < Q_{\mathrm{scattering}}$ at frequencies ≥6 Hz.

Other studies shown in Fig. 4 assumed a frequency independent Q_P (Scherbaum & Wyss 1990; Hansen *et al.* 2004; Lin *et al.* 2015) or Q_S (Koyanagi *et al.* 1995; Hansen *et al.* 2004). Beneath the Summit

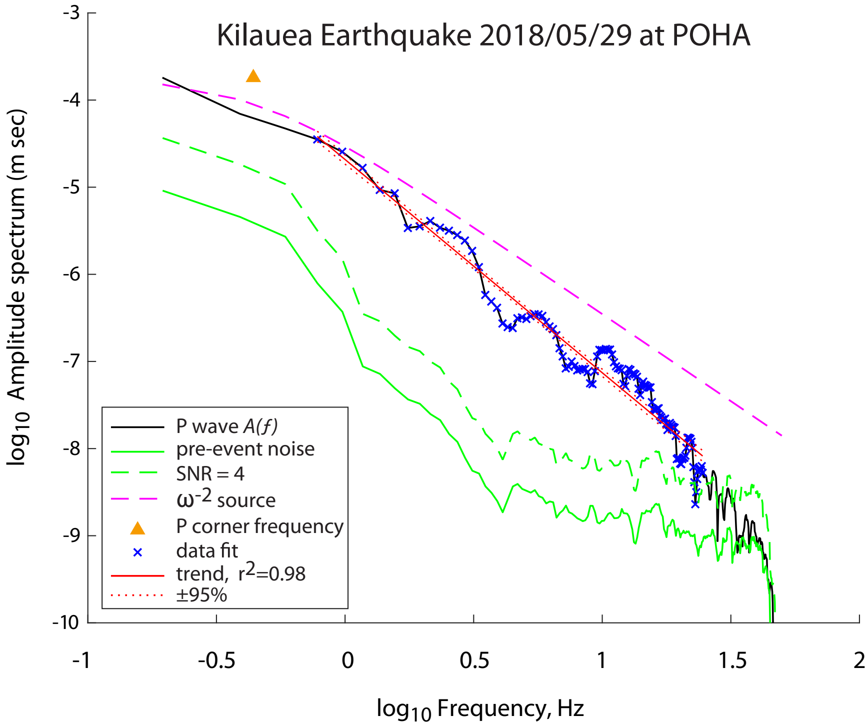

Figure 3. The *P*-wave amplitude spectral data—*A*(f), black curve fit at blue x's—for the May 29 earthquake (M_w 5.3) are fit by a linear trend (red). *S* waves are analysed identically. The corner frequency (orange triangle) is defined by the intersection of the *P*-wave amplitude spectral trend (red) with the amplitude at lowest-frequency (e.g. Hanks & Thatcher 1972). The earthquake ω^{-2} source spectrum is shown (magenta dashed curve) derived from the corner frequency. The solid green curve is the pre-event noise level, where the dashed green curve shows the minimum SNR of 4. The effective Q is measured from the amplitude decrease of the data with respect to the ω^{-2} source level.

at shallow depths (0–3 km) Lin *et al.* (2015) find the Q_P values range between 30 and 105, and at 12 km depth below the Summit a Q_P of 310. In general, the compressional wave attenuation met or exceeded that for shear waves.

5 PROPAGATION OBSERVATIONS

5.1 Halema‘uma‘u to Pohakuloa

Effective Q observations between 1 and 38 Hz at POHA are presented in Fig. 5. Both Q_P and Q_S show similarities: (1) Q values are lowest (~100) at low frequency, ~1 Hz; (2) from 2 to 8 Hz effective Q increases to a range 200–300; (3) there is a relatively sharp increase in effective Q to ~500 between 8 and 10 Hz; (4) at frequencies above 10 Hz, effective Q shows an increasing trend in Q_S and decreasing trend in Q_P—although not independent of frequency, the trends show only a modest frequency dependence and (5) fitting linear trends to the effective Q, $\frac{\mathrm{d}Q_s}{\mathrm{d}f} = 1.7$ and $\frac{\mathrm{d}Q_p}{\mathrm{d}f} = -4.3$.

Using the relationship between seismic velocity (V_P and V_S) and complex moduli (K and μ), wherein $Q_s \equiv Q_\mu$, the complex modulus of rigidity is derived from V_S, whereas the complex modulus of incompressibility K is derived from V_P and V_S. By calculating Q_K I thereby transform Q_s and Q_p into Q_μ and Q_K, separating attenuation losses in shear from losses in compression. The bulk losses generally exceed the shear losses, that is ($Q_K < Q_\mu$). Comparing Q_K in the noted frequency ranges for Q_s and Q_p, (1) Q_K values are lowest (~75) at low frequency, ~1 Hz; (2) from 2 to 8 Hz effective Q_K increases to a range 175–250; (3) there is a relatively sharp increase in effective Q_K to ~400 between 8 and 10 Hz; (4) at frequencies above 10 Hz, effective Q_K decreases and (5) fitting linear trends to the effective Q_K, $\frac{\mathrm{d}Q_K}{\mathrm{d}f} = -2.5$.

5.2 Halema‘uma‘u to KHLH Kahului, Maui

Effective Q measurements from Halema‘uma‘u to KHLH (Fig. 6) are limited by the seismic noise at this coastal Maui site, at frequencies beyond 18 and 13 Hz for Q_P and Q_S, respectively. Nonetheless, $Q_P(f) < Q_S(f)$ at all observed frequencies, and both show a linear trend, wherein $\frac{\mathrm{d}Q}{\mathrm{d}f} \sim 33$. Since $Q_P(f) < \frac{9}{4} Q_S(f)$ at KHLH, the bulk attenuation Q_K is also displayed in Fig. 6. In contrast to POHA, the path to KHLH shows a strong linear frequency dependence. Comparing observations at $f = 10$ Hz, KHLH has generally lower values of Q and thereby higher attenuation than POHA. For POHA Pohakuloa, the observed $Q_P \approx 550$, $Q_S \approx 450$ and $Q_K \approx 300$, whereas for KHLH Kahului, $Q_P \approx 350$, $Q_S \approx 400$ and $Q_K \approx 250$. Interestingly, the subtle variations from a linear trend in Q_P and Qs lead to narrow peaks (lower attenuation) in Q_K just above 6 and 11 Hz, and a trend in $\frac{\mathrm{d}Q}{\mathrm{d}f} \sim 25$.

5.3 Halema‘uma‘u to ALOHA Cabled Observatory

Effective Q measurements at ALOHA (Fig. 7) extend to higher frequencies—beyond 23 and 20 Hz for Q_P and Q_S, respectively—at this deep ocean site than observed at KHLH. Furthermore, $Q_P(f) < \frac{9}{4} Q_S(f)$ as seen at KHLH. Like KHLH, the path to ALOHA also shows a strong linear frequency dependence. However, unlike KHLH, the linear trends differ significantly, $\frac{\mathrm{d}Q_P}{\mathrm{d}f} \sim 34$ (compare KHLH) and $\frac{\mathrm{d}Q_S}{\mathrm{d}f} \sim 46$. Comparing with prior observations at $f = 10$ Hz, ALOHA measures shows higher Q and lower

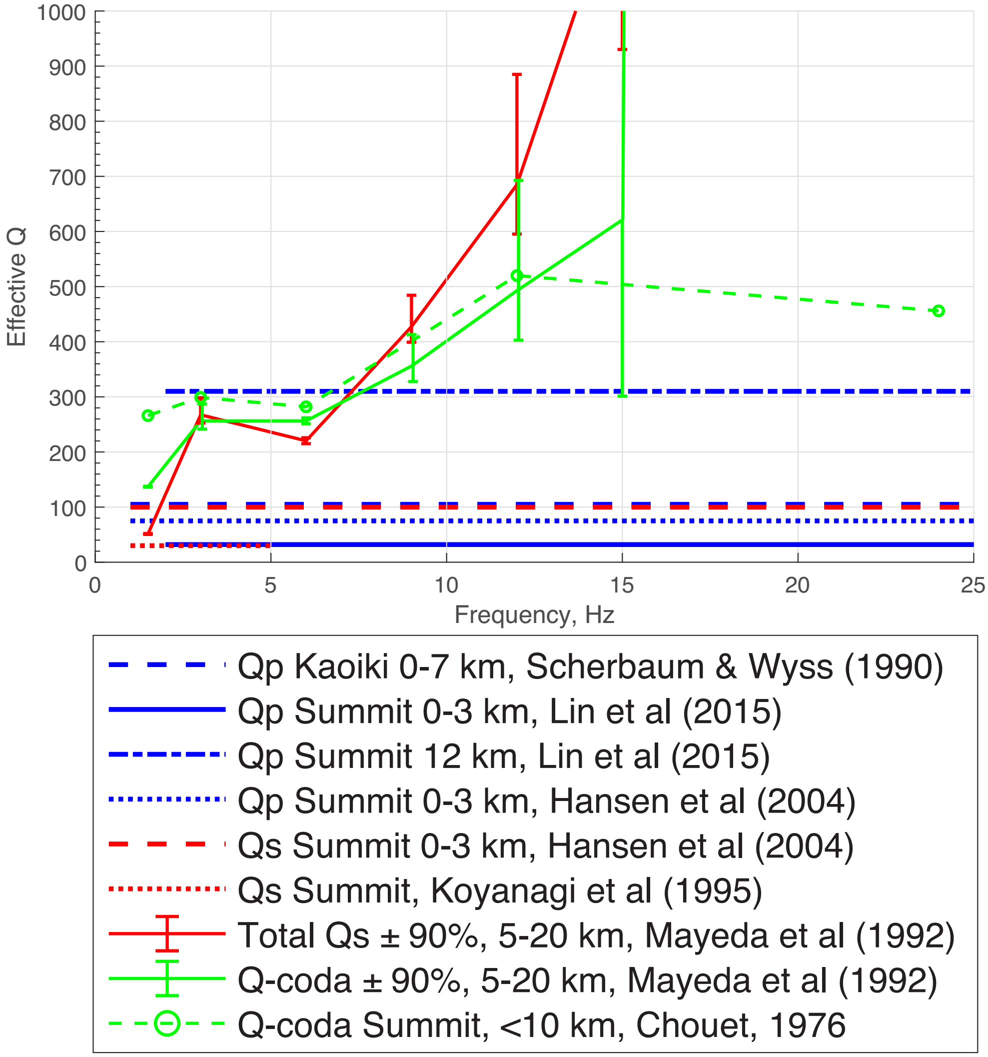

Figure 4. Prior Q studies referenced for the Island of Hawaiʻi are plotted together for Q_P (blue) and Q_S (red). The nominal depth range of the measurements within the focus area is indicated. The Summit refers to Kīlauea. Q-coda (green) is nominally Q_S. The frequency range reflects the data sample rate in the respective study, whether or not the high-frequency content is measured. Data and error bars are truncated at an effective Q of 1000.

attenuation than KHLH: $Q_P \approx 400$, $Q_S \approx 600$ and $Q_K \approx 300$. This observation is an indication that the path from KHLH to ALOHA differs significantly from the initial Halemaʻumaʻu to KHLH segment.

5.4 Beneath Hawaiian volcanos into the oceanic crust

The path to the ACO extends 263 km past KHLH. Initially beneath the distal flanks of Pu`u Kukui and Wailau volcanos (Fig. 1), the path from KHLH to ALOHA first traverses 80 km into Pacific crust beneath the 3000 m bathymetry contour. The last 183 km (70 per cent) of the path is in the oceanic crust—sampled by the ALOHA hydrophone at ACO at 4728 m water depth.

The effective Q measurements at ALOHA linearly increase with frequency where $Q_S > Q_P > Q_K$ over the frequency band. Unlike KHLH where the slope $\frac{\mathrm{d}Q_S}{\mathrm{d}f} \cong \frac{\mathrm{d}Q_P}{\mathrm{d}f}$ for ALOHA $\frac{\mathrm{d}Q_S}{\mathrm{d}f} \cong 1.3\frac{\mathrm{d}Q_P}{\mathrm{d}f}$, indicating higher Q_S within the oceanic crust. As the propagation to ALOHA has 43 per cent overlap with the KHLH path, Fig. 8 plots Q for both sites. $Q_{S\,\mathrm{ALOHA}} > Q_{S\,\mathrm{KHLH}}$ except below 2.5 Hz where $Q_{S\,\mathrm{ALOHA}}$ is more attenuating. $Q_{P\,\mathrm{ALOHA}} \approx Q_{P\,\mathrm{KHLH}}$ except between 7 and 11 Hz where $Q_{P\,\mathrm{ALOHA}} > Q_{P\,\mathrm{KHLH}}$. In general, $Q_{K\,\mathrm{ALOHA}} \approx Q_{K\,\mathrm{KHLH}}$. However, the source of two narrow Q_K peaks near 6 and 11 Hz peaks is a mystery. Bulk attenuation continues unabated beyond KHLH to ALOHA, indicating that the bulk loss mechanism operating within the Hawaiian volcanos, appears as well in the thickened crust (Leahy *et al.* 2010) north of Oʻahu. In summary the effective Q's observed at KHLH are comparable to those at ALOHA for Q_P and Q_K, whereas Q_S is substantial higher at ALOHA.

Following equations (5)–(7) I have derived the attenuation relevant to the path from KHLH to ALOHA by assuming that the energy observed at the surface of Maui is a reasonable proxy for the energy propagating at depth beneath Maui. Since the high-frequency noise at KHLH is higher than at ALOHA, the full frequency content out to ~22.5 Hz observed at ALOHA cannot be corrected. Fig. 9 plots the effective Q for the KHLH–ALOHA path segment. For prior comparisons (Figs 5–7) at $f = 10$ Hz, the KHLH$\longrightarrow$ALOHA segment measures $Q_P \approx 300$, $Q_S \approx 1250$ and $Q_K \approx 500$. $\frac{\mathrm{d}Q_P}{\mathrm{d}f} \sim 30$ (compare KHLH) and $\frac{\mathrm{d}Q_S}{\mathrm{d}f} \sim 138$, and $\frac{\mathrm{d}Q_K}{\mathrm{d}f} \sim 31$. Note the substantial increase of Q_S within the oceanic crust, as compared with the paths within the volcanic edifice.

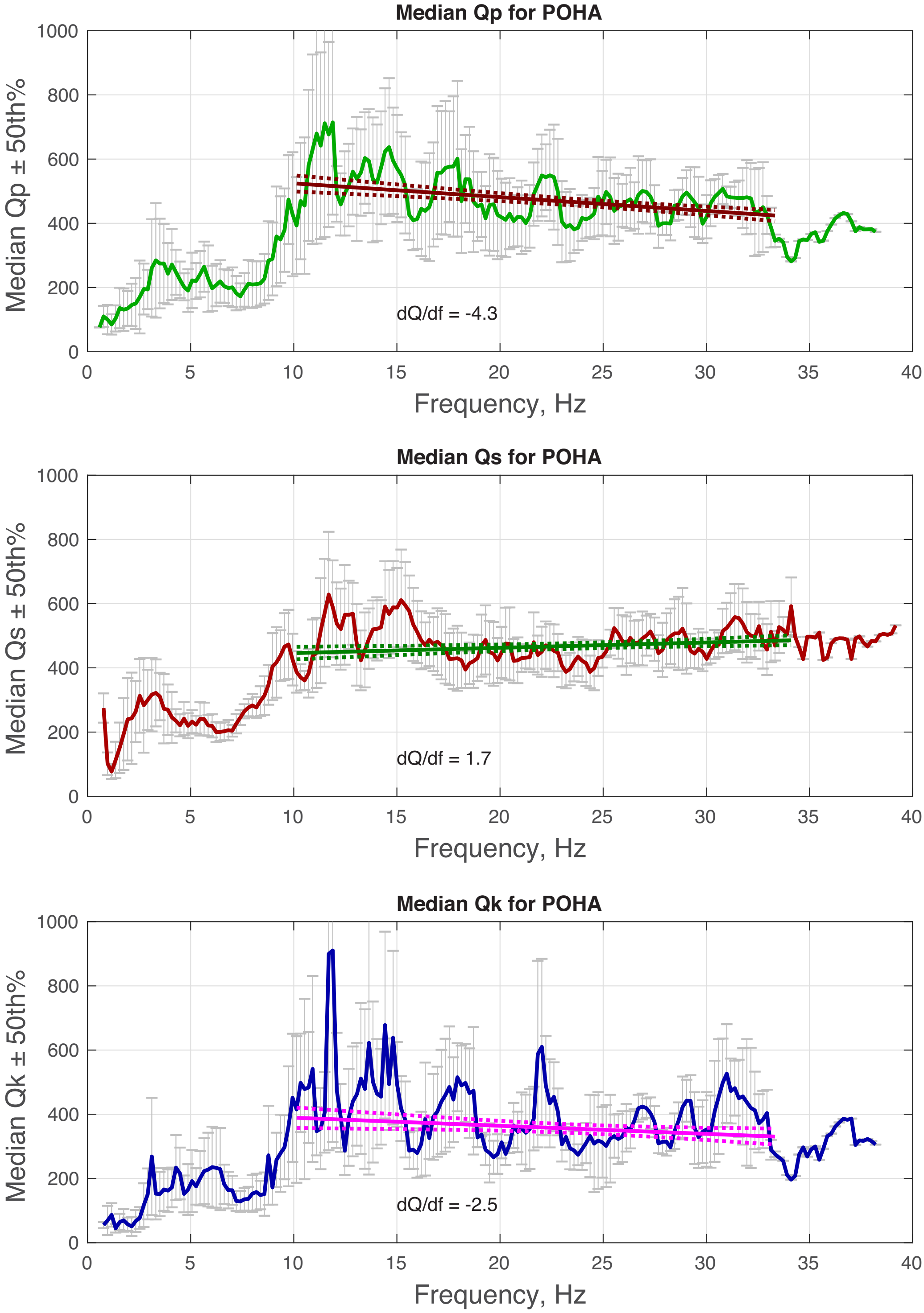

Figure 5. The effective Q are shown for the path from Kīlauea Summit to POHA, Pohakuloa on the saddle between Mauna Loa and Mauna Kea. As the compressional wave Q_P is sensitive to attenuation losses in both shear (rigidity μ) and compression (bulk K) moduli, the Q_K is derived from Q_P and Q_S. Note that $Q_\mu \equiv Q_S$. The top, middle, and lower panels refer to effective Q_P (green), Q_S (red) and Q_K (blue), respectively. At each frequency the median effective Q are plotted and the error bounds refer to the median absolute deviation of the sample population (the 25–75 percentiles, attributed as ±50 per cent). The effective Q are remarkably similar: initially increasing with frequency up to about 10 Hz, then leveling off wherein both Q_P and Q_S show the same nominal range of Q between 400 and 600. Q_P and Q_K decline moderately for $f > 10$ Hz, whereas Q_S increases moderately. $\mathrm{d}Q/\mathrm{d}f$ slopes are marked for the linear trend lines with 95 per cent confidence intervals (dotted). In this single plot several differing attenuation processes are shown: Q_μ, Q_K, $Q \sim f$ and Q nominally constant.

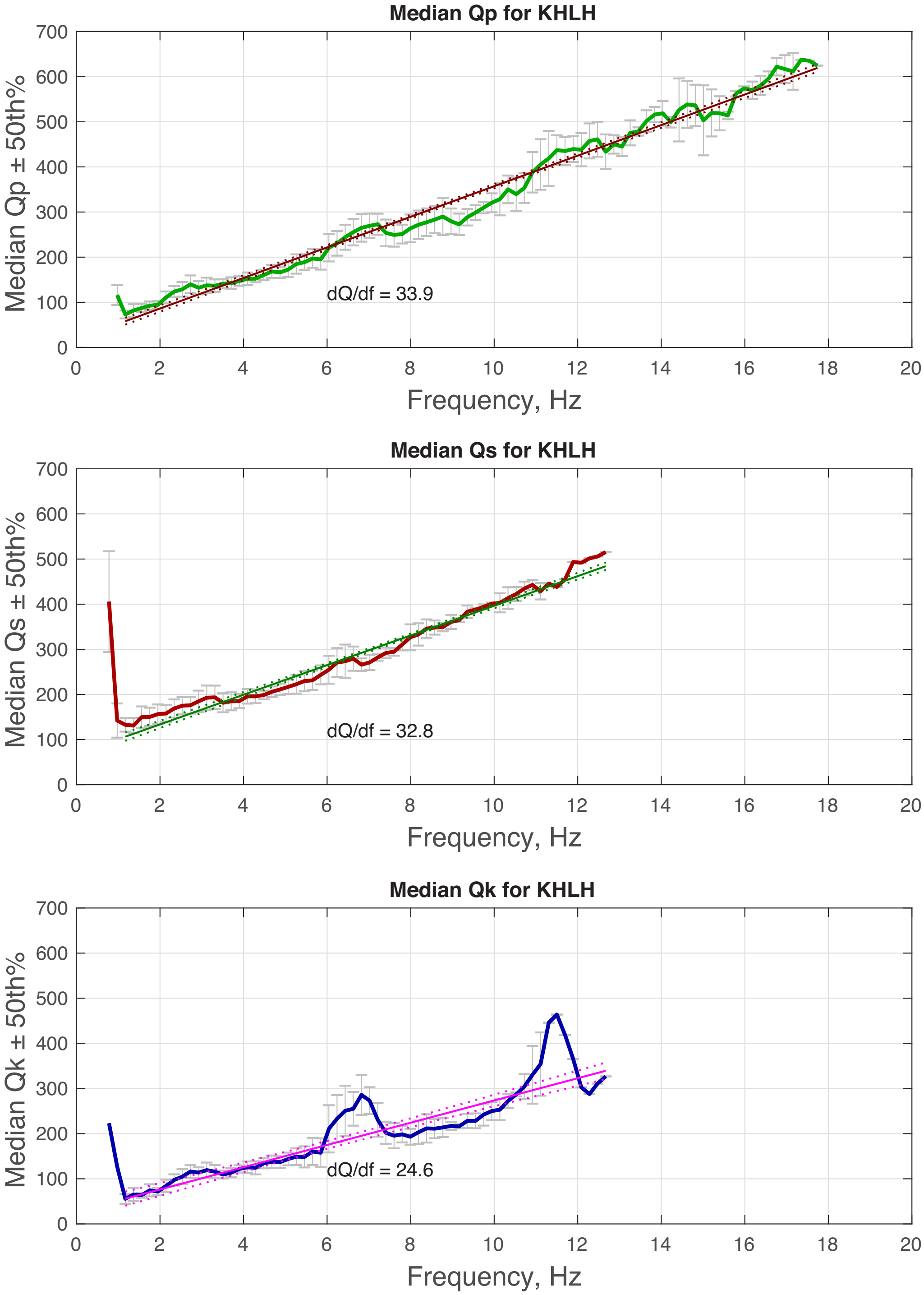

Figure 6. The effective Q are shown for the path from Kīlauea Summit to KHLH, Kahului, Maui. The format follows Fig. 5. Over this path $Q_P < Q_S$ though $\mathrm{d}Q/\mathrm{d}f \sim 33$ for both. As before, Q_K is derived from Q_P and Q_S. There are two Q_K peaks just above 6 and 11 Hz, which appear from subtle features of Q_P and Q_S. As these peaks represent lower attenuation, it is not obvious why Q_K would increase in these narrow bands. At low frequency near $f = 1$, Q rises sharply in each panel. These high values are observed for many events, and are a robust feature, though the amount of increase varies substantially.

Several observations may immediately be drawn. $Q_{P\,\mathrm{KHLH}\rightarrow\mathrm{ALOHA}} \approx Q_{P\,\mathrm{KHLH}}$ and share the nearly the same $\frac{\mathrm{d}Q_P}{\mathrm{d}f} \approx 32$. $Q_{S\,\mathrm{KHLH}\rightarrow\mathrm{ALOHA}}$ exceeds all other effective Q's observed herein, increasing rapidly from 4 to 11 Hz with $\frac{\mathrm{d}Q_S}{\mathrm{d}f} \cong 138$; at 11 Hz $Q_{S\,\mathrm{KHLH}\rightarrow\mathrm{ALOHA}} \approx 1500$. Nonetheless, the effective $Q_{S\,\mathrm{KHLH}\rightarrow\mathrm{ALOHA}}$ also increases to ∼1000 at 3 Hz. For bulk attenuation $Q_{K\,\mathrm{KHLH}\rightarrow\mathrm{ALOHA}}$ the linear trend grows at the same rate as $Q_{P\,\mathrm{KHLH}\rightarrow\mathrm{ALOHA}}$. Further, since

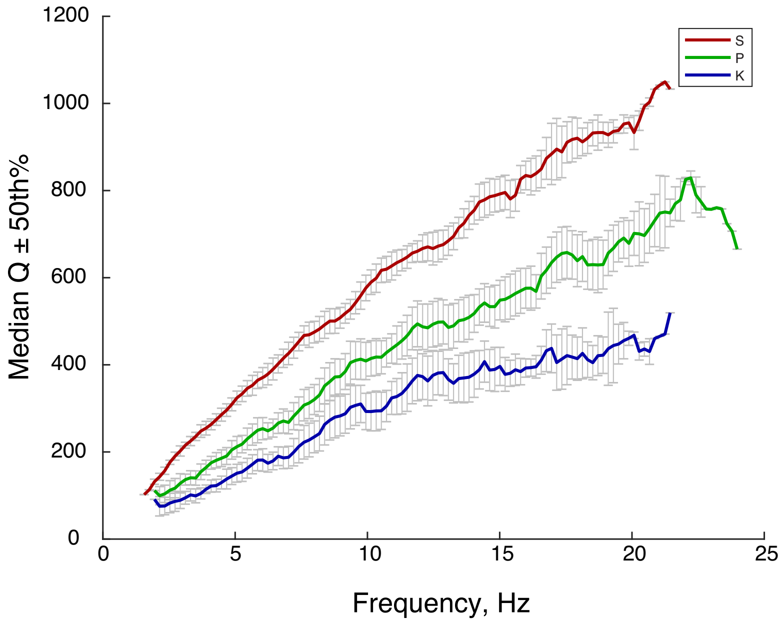

Figure 7. Median effective Q are shown for the path from Kīlauea Summit to the Aloha Cabled Observatory (ACO). The format follows Fig. 5, but is arranged to clearly show $Q_S > Q_P > Q_K$ over the frequency band. Over this 465 km path, $Q_S > 1000$ above 20 Hz. Nonetheless, this path includes the high attenuation near Kīlauea, and therefore must be higher still over a path segment from KHLH to ALOHA. Linear trends (not plotted for clarity) indicate $\mathrm{d}Q/\mathrm{d}f$ of 34.5 (Q_P), 45.8 (Q_S) and 21.6 (Q_K). Error bounds are 50 per cent intervals based on median absolute deviation.

$Q_{S\,\mathrm{KHLH}\rightarrow\mathrm{ALOHA}} \gg Q_{P\,\mathrm{KHLH}\rightarrow\mathrm{ALOHA}}$, the losses in rigidity are smaller and thereby contribute less to Q_P which trends with $Q_{P\,\mathrm{KHLH}\rightarrow\mathrm{ALOHA}} \approx Q_{K\,\mathrm{KHLH}\rightarrow\mathrm{ALOHA}}$.

6 BULK ATTENUATION

The observation of significant bulk attenuation is unusual. All global earth models have $Q_K \gg Q_\mu$, although some bulk attenuation is required to fit the lowest order radial modes (${}_0S_0 - {}_0S_6$) of the Earth's free oscillations (Knopoff 1964; Anderson 1980; Dziewonski & Anderson 1981; Widmer *et al.* 1991; Dahlen & Tromp 1998; Romanowicz & Durek 2000). Anderson (1980) proposed Q_K in the inner core, though noted that $Q_K \sim 10\,000$ throughout the Earth can match the data. Durek & Ekstro¨m (1996) presented earth models where Q_K is expressed solely in the upper mantle ($Q_K \sim 1060$) or within the asthenosphere (80–220 km depth) $Q_K \sim 175$. For crustal propagation in and near Hawai‘i $Q_K \sim 75$ (Figs 6 and 7) at frequencies near 1 Hz. However, the primary data for the radial modes are very long period, where $T \geq\sim 1000$ s. Therefore, any oceanic crustal contribution to the Q_K for ${}_0S_0$ attenuation requires substantially broader relaxation times than observed in this study.

Shifting four decades in frequency, Butler *et al.* (1987) measure Q_P and Q_S at frequencies from 2.5 to 22.5 Hz near Wake Island. The data set are P_o and S_o (nomenclature for long-range, high-frequency *Pn and Sn* from Walker & McCreery 1987) propagating in the west-central Pacific crust and lithosphere along a 1500-km ocean-bottom hydrophone linear array. In this experiment shear waves showed significantly higher frequencies than compressional wave energy, which is modelled as $Q_P < Q_S$. Bulk attenuation derived shows Q_K increasing with frequency as $f^{0.5}$ from ~200 to 800. Therefore, the results here confirm the existence of bulk attenuation in the shallow Pacific lithosphere at frequencies >2 Hz.

Wei & Wiens (2020) modelled attenuation in the upper mantle of the Lau Basin using the basic f^{-2} earthquake source spectrum methodology presented herein (Fig. 3). Significant differences in the Wei & Wiens (2020) approach include: (1) 952 mantle earthquakes were analyzed at depths 50–700 km; (2) P-wave SNR > 2 and SNR > 1.8 for S waves; (3) the nominal frequency bands are 3 to ~14 Hz for P waves and 1 to 4 Hz for S waves and (4) the intrinsic Q_P and Q_s are independent of frequency. The lowest, derived mantle Q_μ and Q_K are ~28 and ~21, respectively, and occur beneath the Lau backarc spreading. The Q values are significantly less than the minimum crustal Q's observed herein (Fig. 5) where Q_μ and Q_K are ~85 and ~50, respectively. Wei & Wiens (2020) ascribe the bulk attenuation as ‘caused by one or more mechanisms related to partial melt, including porous melt flow through interconnected pores and incremental stress-induced changes in melt fraction.’

In principle, some of the compressional losses ascribed to Q_K may be due to $Qp_{\mathrm{scattering}}$. The ratio of P to S wavelengths is $\sqrt{3}$ for a Poisson solid. Thus, the scale-length of scattering at $f = 10$ Hz for S waves would occur at ~17 Hz for P waves. For crustal measurements, $Q_{\mathrm{scattering}} > Q_{\mathrm{intrinsic}}$ for S waves observed in Hawai‘i (Chouet 1976; Mayeda *et al.* 1992), Japan (Carcolé & Sato 2010; Takahashi 2012; Takemura *et al.* 2017) and the contiguous United States (Eulenfeld & Wegler 2017). Hence, at a given frequency f, $Q_K(f)$ is derived from $Q_P(f)$ and $Q_S(f)$, whereas $Qp_{\mathrm{scattering}}(\sqrt{3}f)$ and $Qs_{\mathrm{scattering}}(f)$ have differing frequency dependencies. Since we have little constraint on the P-wave scattering, I assume for simplicity that $Qp_{\mathrm{scattering}} > Qp_{\mathrm{intrinsic}}$ and that the contribution of $Qp_{\mathrm{scattering}}$ has only a minor effect on Q_K.

6.1 Q_K Mechanism

Bulk attenuation can arise from the mismatch in bulk medium properties (Budiansky & O'Connell 1980)—incompressibility K, coefficient of volumetric thermal expansion α_V, thermal conductivity κ, thermal diffusivity α_D. Anderson (1989) states, ‘If

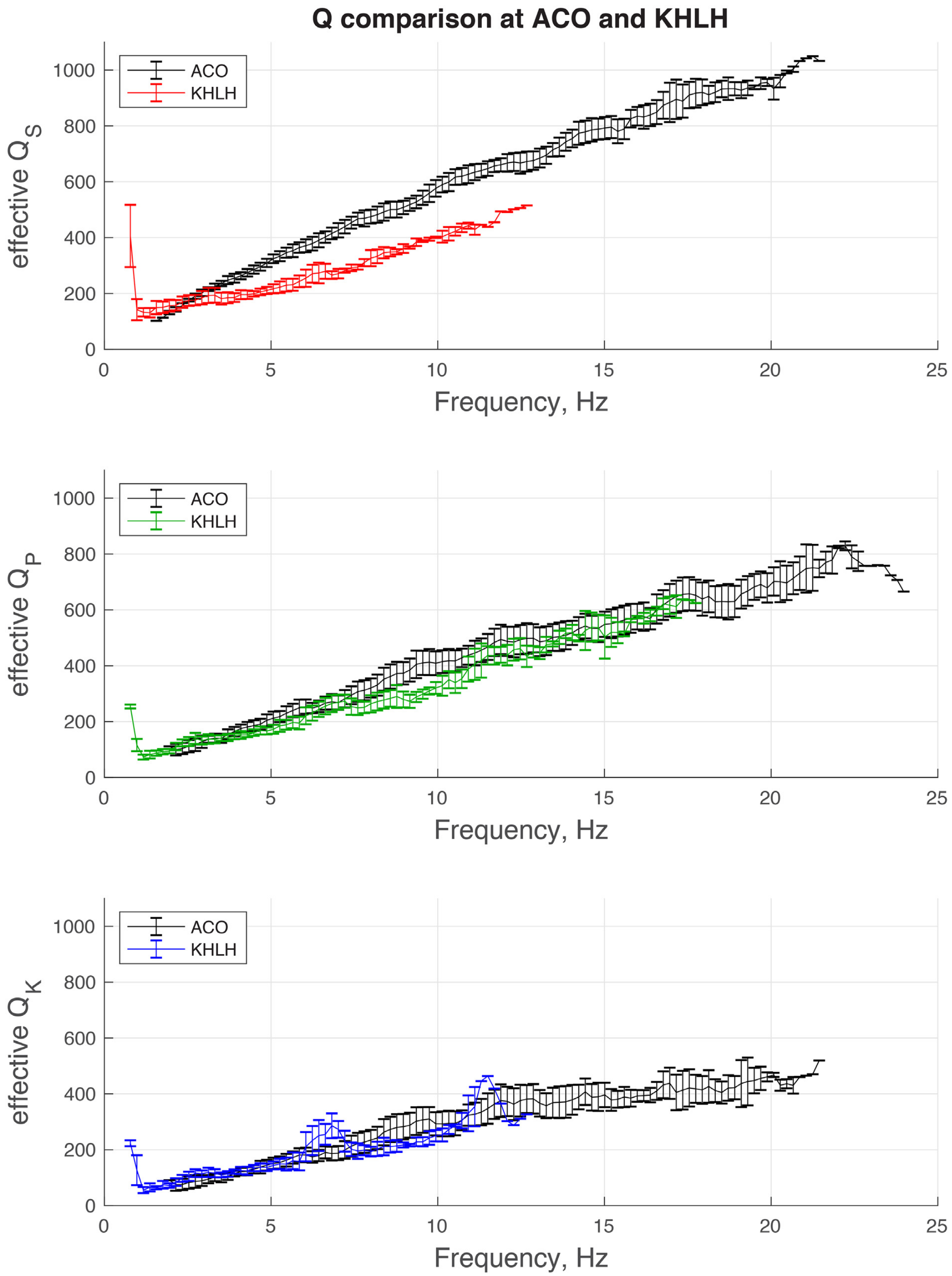

Figure 8. Q_P, Q_S and Q_K are shown comparing the volcanic traverse to KHLH with the same traverse extending via oceanic crust out to ACO. The ALOHA data are shown in black, and the KHLH data in colour. The trends observed for Q_P and Q_K in the middle and lower panels substantially coincide, indicating that the attenuation environment in the ocean crust is comparable to the volcanic traverse. However, in the upper panel the oceanic Q_S path shows significantly lower attenuation, $Q_{S\mathrm{ALOHA}} > Q_{S\mathrm{KHLH}}$.

a composite contains grains that are very anisotropic or differ greatly in their properties, the bulk attenuation can be substantial. For a factor of 2 contrast in the coefficient of thermal expansion or bulk modulus, Q_K can be as low as 300 and 3000, respectively (Budiansky & O'Connell 1980).' Here, the analog is the water saturated vesicles in a basalt medium. Hence, the passage of seismic energy through water-saturated vesicular basalts can, in principle, loose energy to heat through the differential strains acting on the contrasting media properties. The principal dichotomies in these properties are shown by the following ratios (basalt/water): bulk modulus (25), volumetric thermal expansion (1/16), thermal conductivity (3) and thermal diffusivity (7). Experimental measurements of water saturated basalts (Batzle *et al.* 2014) have found Q_K decreasing (20 to 11) over the fre-

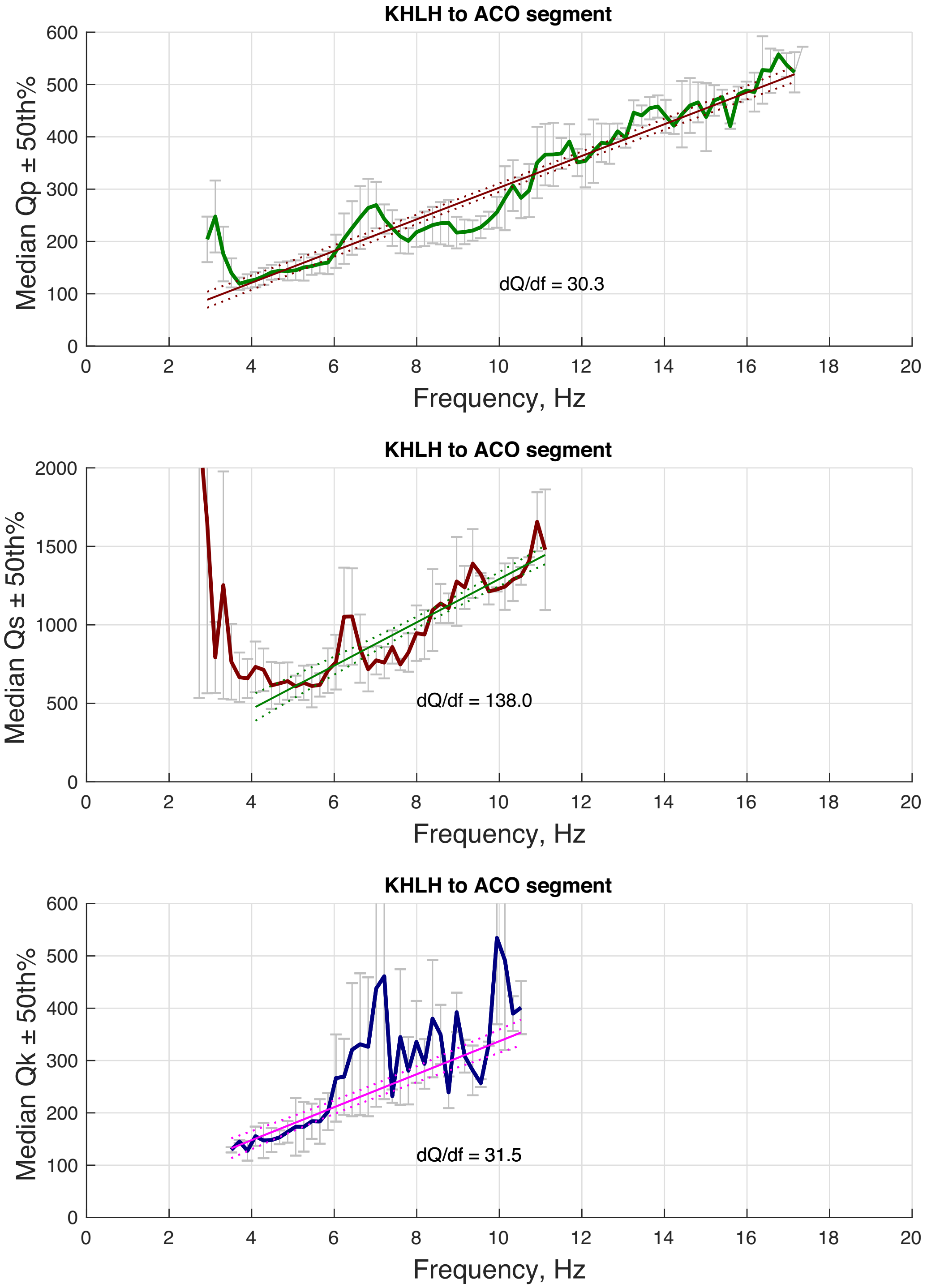

Figure 9. The path to ALOHA, Aloha Cabled Observatory follows nearly the same path to KHLH as the Hawaiian volcanos traverse (Fig. 1). The incremental attenuation over the path from KHLH to ALOHA is calculated and shown here. Note that the frequency range is limited by noise levels at the coastal KHLH site, as well as the requirement to derive Q from earthquakes mutual to each site. Q_S reaches 1500 at 11 Hz. Extending the trend linearly to 20 Hz (as in Figs 8 and 9), the possible attenuation for the KHLH$\longrightarrow$ALOHA segment would potentially reach $Q_S \sim 2750$. Further, the bulk attenuation seen for the volcanic paths is again observed for this oceanic segment. Near Wake Island, Butler *et al.* (1987) derived both high $Q_S \sim 3000$ at 20 Hz, and significant bulk attenuation Q_K. However, both Q_P and Q_K observed near Wake Island shows lower attenuation than observed herein.

quency (2–25 Hz) and then increasing to $Q_K = 20$ again toward 350 Hz.

Without fully deriving the relative effect of contrasting properties between basalt and a water-filled vesicle, the basic effect of relative temperature change to small pressure change can illuminate the process. Following Castellan (1964) $P\bar{V} = RT$, and the temperature derivative with respect to pressure is $\mathrm{d}T = \bar{V}\mathrm{d}P/R$, where $\bar{V}$ molar volume and R is the universal gas constant

(8.314 J mole^{-1} $^{\circ}K^{-1}$). Based on an average of 53 analyses of olivine basalts from the Hawaiian Islands (Volcanoes of the National Parks of Hawai‘i 2006), the molar volume of basalt is $\bar{V} \cong 2.1 \times 10^{-5}$ m^3 mole^{-1}; for water, $\bar{V} \cong 1.8 \times 10^{-5}$ m^3 mole^{-1}. Hence, $\mathrm{d}T = \bar{V}\mathrm{d}P/R \approx$

$$\begin{aligned} \Delta T_{\text{basalt}} &\cong 2.5 \times 10^{-6} \Delta P_{\text{basalt}} \\ \Delta T_{\text{water}} &\cong 2.2 \times 10^{-6} \Delta P_{\text{water}} \end{aligned}. \tag{8}$$

For the same pressure change ΔP in S.I. units,

$$\frac{\Delta T_{\text{basalt}}}{\Delta T_{\text{water}}} \cong 1.14. \tag{9}$$

Therefore, a unit change in pressure affects a change in the temperature of the basalt 14 per cent more than that of water, causing heat to flow across the water–basalt boundary to return to equilibrium.

6.2 Vesicles

A phenomenological case is made that the presence of basalt vesicles (porosity), saturated with water, is a potential source for the shallow bulk attenuation. The existence of vesicles is evident at the surface of Hawaiian volcanos (e.g. Walker 1989). The Hawai‘i Scientific Drilling Project (HSDP, Garcia *et al*. 2007) drilled to a depth of 3.1 km near Hilo, Hawai‘i, into both Mauna Kea and Mauna Loa; and the Hawai‘i Scientific Observation Hole 1 (SOH1, Garcia *et al*. 2007) drilled into 1.7 km into the Kilauea east rift zone (ERZ). Median vesicle (vol. per cent) in subaerial flow units range from 4 to 18 per cent. The mean observed vesicle abundance in the submarine cores from Mauna Kea and the Kīlauea ERZ were 3.4 and 6.7 per cent by volume.

The Ocean Drilling Project (ODP) has sampled the upper crust of the Pacific over many of its legs. ODP Hole 801C was drilled in 160 Ma, Jurassic crust 1000 km west of Wake Island into basalt basement from 480 to 594 m below sea floor (mbsf), finding apparent bulk porosities from 1 to 23 per cent (Larson *et al.* 1993). In the easternmost equatorial Pacific Slagle & Goldberg (2011) report porosities from ODP sites 1256 and 504. Site 1256 was drilled 1257 m into basement penetrating 15 Ma crust; Site 504 penetrated 1836 m into basement in 6.9 Ma crust. Porosity measurements (from both resistivity and seismic velocity) for Site 504 ranged from 5 to 24 per cent; at Site 1256 from 3 to 37 per cent. Between the Murray and Molokai Fracture Zones ODP site 1224 at the H2O observatory (Butler *et al.* 2000) was drilled into 46 Ma basaltic oceanic crust to a depth of 175 mbsf between the Murray and Molokai Fracture Zones (Kasahara & Stephen 2006). Porosities of 4–15 per cent and higher were reported. Thus, at widely differing sites and sea floor ages within the Pacific, vesicular basalts are evident in the upper crust, with porosity values comparable to those observed within the Island of Hawai‘i.

7 SHEAR WAVE ATTENUATION

Shear wave energy losses are potentially due to a multitude of mechanisms, which were broadly outlined by Anderson (1967) and Jackson & Anderson (1970). These include: dislocations (relaxation, resonance, hysteresis, stress induced diffusion and creep), thermoelastic relaxation, grain-boundary damping, transient coldwork internal friction, deformation hysteresis and point defect internal friction, among others. Although we cannot resolve the actual attenuation mechanism(s), we can constrain a key property, the activation energy.

7.1 Activation energy

Many attenuation mechanisms are activated by temperature and pressure,

$$Q_1\,(T_1, P_1) = Q_0 \;\exp \frac{E^* + \bar{V} P_1}{RT_1}. \tag{10}$$

I have derived the attenuation Q_S for shallow basalt (measured at POHA) and a mid-crustal basaltic composition (measured at KHLH), and therefore can relate the ratio of Q’s to the ratio of exponentials for appropriate temperature and pressure along the path. Let (T_1, P_1) be measured shallow at POHA and (T_2, P_2) over crustal KHLH path, E^* is the activation energy and $\bar{V}$ the molar volume

$$\frac{Q_1\,(T_1, P_1)}{Q_2\,(T_2, P_2)} = Q_0 \exp \frac{E^*+\bar{V}P_1}{RT_1} \Big/ Q_0 \exp \frac{E^*+\bar{V}P_2}{RT_2} \tag{11}$$

After some algebra,

$$E^*_{\text{basalt}} = \frac{RT_2T_1\;log\left[\frac{Q_1(T_1,P_1)}{Q_2(T_2,P_2)}\right] + \bar{V}(T_1P_2 - T_2P_1)}{(T_2 - T_1)} \tag{12}$$

where R is the gas constant (8.314 J mole^{-1} $^{\circ}K^{-1}$), $\bar{V}$ is molar volume (2.1×10^{-5} m^3 mole^{-1}. P_1 and P_2 are measured at 1 and 6 km depths, respectively, from PREM (without ocean, Dziewonski & Anderson 1981) at 2.5×10^7 and 1.5×10^8 Nm^{-2}, respectively. Temperature (°K) is derived from boreholes at the Pohakuloa Training Area (PTA2, Jerram *et al.* 2019) near POHA and from the Hawaii Scientific Drilling Project (HSDP, Stolper *et al.* 2009). For PTA2 the mean of temperatures between 1 and 1.5 km is 80 °C. This high temperature is corroborated by 3-D magnetotelluric profiles over 500 km^2 showing a broad, low resistivity zone in the saddle between Mauna Loa and Mauna Kea (Thomas *et al.* 2015). The HSDP borehole is near Hilo on the distal flanks of Mauna Loa and Mauna Kea, thereby representative of the distal flanks of other volcanos along the path flor Kīlauea to KHLH. At HSDP I extrapolate conductive and advective temperature gradients from 3 to 6 km (D. Thomas, personal communication, 2019; Stolper *et al.* 2009), yielding $T_{\text{conductive}} = 91\,^{\circ}$C and $T_{\text{advective}} = 112\,^{\circ}$C. For the POHA/KHLH paths, $Q_{SKHLH} < Q_{SPOHA}$ between 1.5 and 5.7 Hz (Fig. 10), where a Q_S ratio of 1.4 fits within the 50 per cent median absolute difference of ratios, when measured at mutual frequencies for the same earthquakes for both paths. Evaluating eq. (11) for a mean $T_2 = 105.5\,^{\circ}$C, the apparent activation energy for shear attenuation in basalt, $E^*_{\text{basalt}} \cong 50$ kJ mol^{-1}. The largest uncertainty lies in the extrapolation of temperature at HSDP and its relevance to the mid-crust between Kīlauea and KHLH. For a temperature range of 91–120 °C, E^*_{basalt} varies from 98 to 34 kJ mol^{-1}.

At shallow depths the $\bar{V}P$ (at 1 km) $= 0.53$ kJ and therefore $E^*_{\text{basalt}} \gg \bar{V}P$ at shallower depths (e.g. propagation to POHA) and the effect of pressure on attenuation is negligible compared with E^*_{basalt}. A corollary for this is that the change in attenuation behaviour at POHA for $f > 10$ Hz, is not simply a shift in Q due to pressure. Rather, the relative frequency independence of $Q(f > 10)$ may be ascribed to a different loss mechanism that limits the observed increase in effective $Q \sim f$ to frequencies below 10 Hz.

For comparison with olivine—at $T = 800$–$1200\,^{\circ}$C for grainsize-sensitive, viscoelastic relaxation in melt-free specimens—Jackson & Faul (2010) report $E^*_{olivine} = 360$ kJ mol^{-1}. For creep and dislocation climb in olivine, Kohlstedt *et al.* (1976) and Goetze (1978) report $E^*_{\text{olivine}} = 523$–$690$ kJ mol^{-1}.

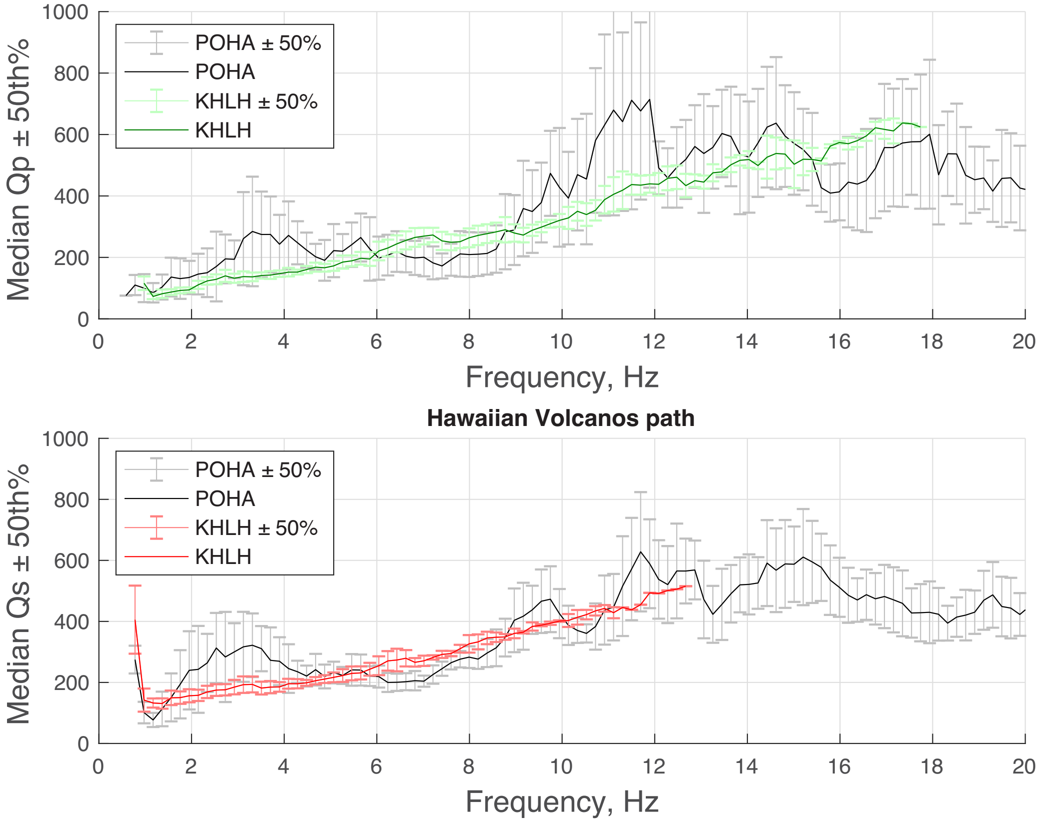

Figure 10. Q_P and Q_S are shown for both paths traversing Hawaiian volcanos, to POHA and to KHLH. The frequency range is abridged from Figs 5 and 6 to enhance the relationships. KHLH Q_P (upper panel, green) and Q_S (lower panel, red) are plotted with POHA (black). The linear trends expressed for KHLH track the rough trend seen for POHA, and both fit within the error bounds of the trends. The increasing Q values trend line joins with the Q plateau for POHA. For Q_P and Q_S at $f < 12$ Hz the attenuation losses for the shallow, 46 km path to POHA are commensurate with the mid-crustal, 207 km path to KHLH.

7.2 Absorption band Q

Butler (1987) modelled the frequency dependent Q_S data (2.5–22.5 Hz, Butler *et al.* 1987) and Rayleigh wave Q_R data (20–40 s) as a seismic absorption band in the Pacific lithosphere near Wake Island with the high-frequency edge of the band at 5.5 Hz. Here, the Q_S over the path from Kīlauea to KHLH are modelled as a standard linear solid with a single relaxation time τ (Debye peak) fitting the observed linear frequency dependence of Q_S (e.g. Minster 1978a,b)

$$Q^{-1}\ (\omega) = \frac{2Q_{\max}^{-1}\omega\tau}{1+\omega^2\tau^2}\,. \tag{13}$$

The maximum Q^{-1} occurs where $\omega\tau\ =\ 1$. Herein, Q^{-1} is maximum at $f_{\text{Debye}} =\ 1.4$ Hz. The characteristic relaxation time is then 0.11 s. Fig. 11 plots the Debye model of Q^{-1} with the Q_S^{-1} data. As there are no model parameters other than the peak value of $Q_{\max}^{-1}(f_{\text{Debye}})$, the fit is good.

An absorption band fit for the POHA data is not warranted as Q_S increases initially, then levels at $f > 10$ Hz. The ALOHA Q_S data increase with frequency faster than the Debye model predicts. I also show the Debye fit to the KHLH Q_K data, which again appears adequate. Nonetheless, it is not clear that Q_K should manifest a Debye peak at all, since bulk attenuation as discussed earlier is not explicitly a thermally activated process. However, if thermally activated, then its activation energy would be in the range $E^*_{\text{bulk}} \cong$ 62–21 kJ mol^{-1} for its Q_K ratio of 0.6, that is $Q_{K\,\text{POHA}} < Q_{K\,\text{KHLH}}$. Furthermore, Q_K has nearly the same form and f_{Debye} as for Q_S, which is remarkable since losses in Q_K are not typically connected with Q_μ. Finally, whereas the width of the Debye absorption band broadly fit the 1.4–14 Hz data, there is no parameter for tuning of the width of the band. Hence, small scale 'valleys' in the Q spectra cannot be explained as due to additional Debye peaks.

8 SCATTERING *Q*

The observed Q_S and Q_P variations (Fig. 5) over the 46-km, Kīlauea–POHA path for $f > 10$ Hz are approximately constant with an imposed 'structure.' The peaks and valleys vary systematically with frequency as observed through the median filter. Nonetheless, the width of the valleys (greater attenuation) does not comport with a series of relaxation peaks. As seen in Fig. 5 the absorption band varies over a broader band of frequencies. Without an intrinsic attenuation attribution, I have looked to scattering attenuation as the source of the observed variation via the relationship (e.g. Mayeda *et al.* 1992):

$$\frac{1}{{}_{\text{eff}}Q} = \frac{1}{Q_{\text{intrinsic}}} + \frac{1}{Q_{\text{scattering}}} \tag{14}$$

$Q_{\text{scattering}}$ includes the interference of elastic waves propagating through a variable, layered media. A cross section of the V_P and V_S variation observed (Jerram *et al.* 2019) in the PTA2 borehole (adjacent to POHA Pohakuloa) between 900 and 1500 m depth is consistent with the expectation of constructive and destructive interference. Scattering differs from intrinsic attenuation in that elastic scattering can lead to both energy decrease and increase. Mapping

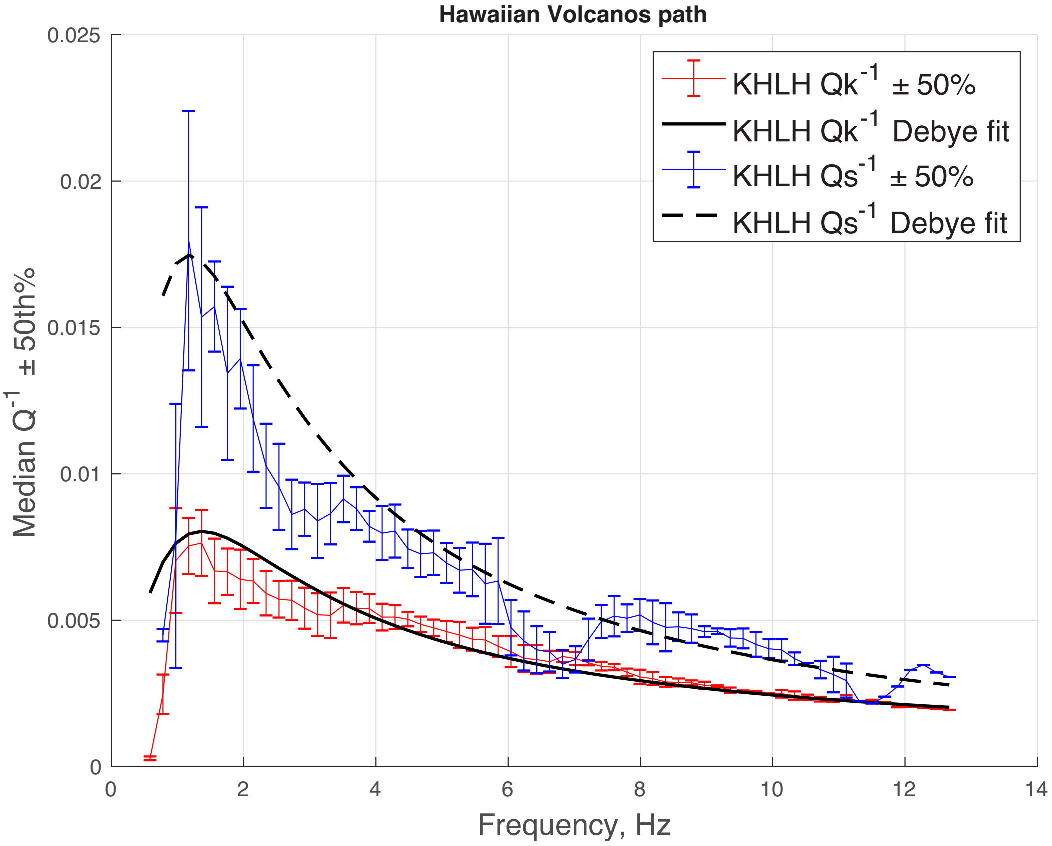

Figure 11. The variation of shear and bulk attenuation—Q_S^{-1}(red) and Q_K^{-1}(blue)—are plotted for the volcano traverse to KHLH. Fitting Debye peaks to the attenuation maxima ($f_{\text{Debye}} = 1.4$ Hz), the fall off with frequency reasonable matches the observed attenuation (solid and dashed black curves). Q_K^{-1} deviates from this trend where the Q_K relative maxima are in Fig. 6.

the scattering variations into Q requires formulating the scattering solely as losses in the context of a frequency independent background intrinsic Q. By example, let $Q_{S\text{intrinsic}} = 650$ from $f = 12 - 33$ Hz. Then the additional scattering losses decrease Q_S. Fig. 12 plots this model, showing that $Q_{S\text{scattering}} \sim 1000$ to 10 000 can explain the variability of Q_S. Similarly for compressional waves $Q_{P\text{intrinsic}} = 700$, then $Q_{P\text{scattering}} \sim 900$ to 7000 can explain the variability of Q_P. For $f > 12$ Hz the shallow scattering wavelengths are $\lambda_P < 450$ m and $\lambda_S < 280$. The levels of scattering attenuation on the Island of Hawai‘i are commensurate with the assessment of Mayeda *et al.* (1992) that $Q_{\text{scattering}} > Q_{\text{intrinsic}}$ at $f > 6$ Hz.

9 BROADER CONTEXT OF EFFECTIVE Q OBSERVATIONS

9.1 Pacific lithosphere

Takeuchi *et al.* (2017) deterministically modelled anelasticity (at ∼3 Hz) in the lithosphere using P_{o} and S_{o} waves from aftershocks of the 2011 Tohoku earthquake on BOBS's deployed on the sea floor of the northwest Pacific. Over a distance range of 7–22°Δ, their preferred lithospheric model shows weak attenuation, $Q_S = 3200$, $Q_P = \frac{9}{4} Q_S$, and stochastic velocity heterogeneity of 2.5 per cent. Shito *et al.* (2013) modelled (up to 5 Hz) P_{o} and S_{o} observed on broad-band ocean-bottom seismometers (BOBS) installed on the northwest Pacific seafloor from subduction earthquakes in Japan. The model qualitatively fitting the P_{o} and S_{o} wave features included $Q_P = Q_S = 1000$ in the crust, $Q_P = Q_S = 2000$ in the upper mantle and stochastic velocity heterogeneity of 2 per cent. Kennett *et al.* (2014) modelled lithospheric intrinsic attenuation and stochastic velocity heterogeneity for P_{o} and S_{o} from earthquakes in Hawai‘i and California (Butler & Duennebier 2000) propagating (2–8 Hz) to the Hawai‘i-2 Observatory, H2O (Butler *et al.* 2000; Butler 2003). Exploring lithospheric $Q_S = 2000$–500 ($Q_P = 2Q_S$), thicknesses of 100 and 50, heterogeneity (0.5–2 per cent) and with crustal $Q_S = 200$, Kennett *et al.* (2014) qualitatively match P_{o} and S_{o} wave features.

Butler *et al.* (1987) modelled the decay of P_{o} and S_{o} from a Kuril Island earthquake. A 1500-km, linear array of 9 ocean bottom hydrophones (the first 4 primarily analysed had an aperture of 422 km) were deployed for two months near Wake Island in 1981 recorded a magnitude M_{w} 6.5 earthquake at an 7° angle to the trend of the array. Both P_{o} and S_{o} were observed with frequencies exceeding 25 Hz arrived at group velocities of 8.2 and 4.7 km s^{-1}, respectively. Peak energies traveled at 7.7 and 4.5 km s^{-1}, which are mid-deep crustal velocities. Attenuation was determined using the classic two-station method, tracing the energy in successive group-velocity windows. Peak Q values of P_{o} and S_{o} reach about 1500 and 4000, respectively. That $Q_P < \frac{9}{4} Q_S$ is an indication of bulk attenuation and/or that P_{o} propagates as a leaky mode. The effective Q's for P_{o} and S_{o} increase with frequency: for P_{o}, $Q_p \sim f^{0.7}$ from about 300 at 2.5 Hz to 1500 at 17.5 Hz; for S_{o}, $Q_S \sim f^{1.1}$ from about 400 at 2.5 Hz to 3000 at 22.5 Hz.

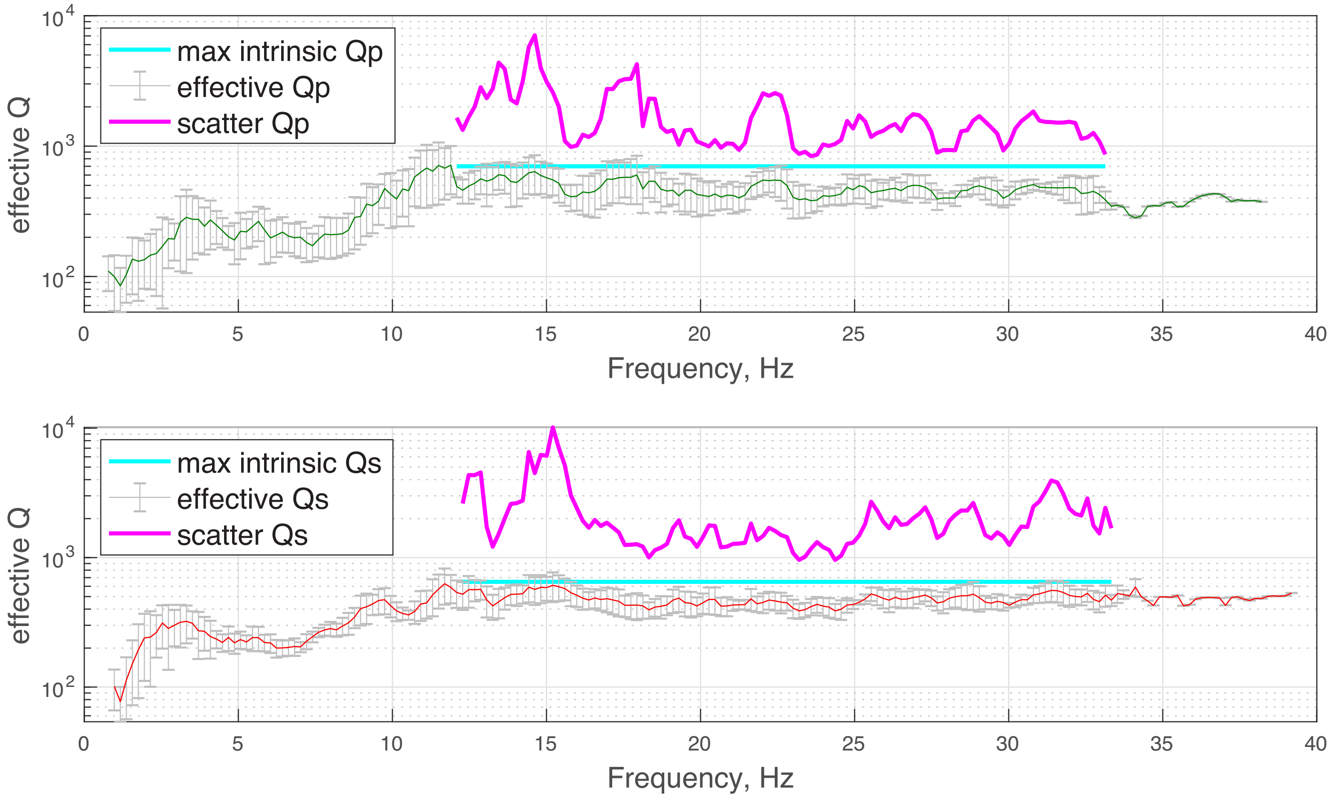

Figure 12. Fluctuations in effective Q at POHA Pohakuloa are modelled as variation with elastic scattering. Median Q_P (upper panel) and Q_S (lower panel) from Fig. 5 are plotted with error bounds. Assuming that Q is frequency independent from 12 to 33 Hz (cyan line), the amount of $Q_{\text{scattering}}$ needed to produce the observed $Q_{\text{intrinsic}}$ fluctuations are shown by the magenta lines. Note logarithmic Q scale.

Table 1. Comparison of *Q*(*f*) observed over two separate oceanic paths.

Effective Q (frequency range, Hz)	KHLH⟶ALOHA	Wake
Q_p (3)	200	300
Q_p $(4-17)$	130–550	450–1500
Q_S (4)	800	700
Q_S $(4-11)$	600–1450	700–1600
Q_K $(4-10.5)$	150–400	300–500

The Q values determined for the primarily oceanic KHLH⟶ALOHA path are compared in Table 1 with the Wake Q data set, reflecting the same frequency range for the observations. Summary observations are: (1) In general, the Hawaiian attenuation exceeds that measured near Wake; (2) however, Q_S for the oceanic KHLH⟶ALOHA path differs only moderately compared with Wake; (3) in contrast, Q_p and Q_K are significantly lower than the Wake observations and (4) at a frequencies less than 4 Hz, both Q_P and Q_S increase (lower attenuation) for the KHLH⟶ALOHA path, in contrast to the Wake observations. As an effect of wavelength, this may reflect lower attenuation at greater depth in the crust approaching ALOHA.

9.2 Crustal measurements in Japan and the mainland U.S.

Measurements of high frequency (>1 Hz) intrinsic and scattering attenuation elsewhere place the Hawaiʻi crustal measurements in perspective. Although not an exhaustive list, the following studies are reviewed: in Japan (Carcolé & Sato 2010; Takahashi 2012; Takemura *et al.* 2017) and in the contiguous United States (Eulenfeld & Wegler 2017). In Japan, Carcolé & Sato (2010) measured intrinsic Q_i and scattering Q_{sc} for *S* waves in five 1-octave frequency band (1–32 Hz). The data set was limited to shallow (<40 km depth) earthquakes at distances <100 km. Q_i values ranged from ∼200 to 1500, whereas Q_{sc} ranged from ∼200 to 5000; except at the lowest frequency, $Q_{sc} > \; Q_i$. In northeastern Japan Takahashi (2012) measured *S*-wave effective Q_S—including both intrinsic absorption and wide-angle scattering—in three 1-octave frequency bands (4–32 Hz). The effective Q_S structure shows weak attenuation $_{eff}Q_S(f) \sim 320\,f^{0.5}$ on the forearc side of the volcanic front, and strong attenuation $_{eff}Q_S(f) \sim 200\,f^{0.3}$ (compare Fig. 6) beneath the Quaternary volcanoes and near the collision zone between the Honshu and Kuril arcs. According to the Born approximation, the estimated $_{eff}Q_S$ at 0–40 km depth consists mainly of the intrinsic absorption if the characteristic scale of random inhomogeneities is 5 km or longer. Takemura *et al.* (2017) modelled *P*- and *S*-wave high-frequency seismic wave propagation for distances <150 km for crustal earthquakes in southwestern Japan in three 1-octave frequency bands, 0.5–4 Hz. In these three bands, centered on {0.75, 1 and 3 Hz} the $_{eff}Q_P$ are {400, 100, 100}, and $_{eff}Q_S$ values are {250, 250 and 630}. For the higher frequencies (≥1 Hz) $_{eff}Q_S > {}_{eff}Q_P$. Takemura *et al.* (2017) also found that scattering attenuation due to small-scale velocity heterogeneity has a very small contribution to the observed apparent attenuation, suggesting that intrinsic attenuation is the dominant attenuation mechanism in the crust.

Finally, Eulenfeld & Wegler (2017) use 10 yr of *S*-wave data of the USArray project to estimate attenuation of crustal *S* waves—intrinsic Q_i and scattering Q_{sc}—in the contiguous United States at frequencies between 1.5 and 17 Hz. Earthquakes were limited to depths <40 km, and propagation distance <110 km. Increasing with frequency monotonically, $Q_i \sim 150$ to 1700 and $Q_{sc} \sim 150$ to 2000. For $f > 1.5$ Hz, $Q_{sc} > Q_i$ in the western United States, but comparable in the east, $Q_{sc} \sim Q_i$.

10 DISCUSSION

The study of attenuation of seismic waves from 50 earthquakes colocated in the Halemaʻumaʻu crater of Kīlauea's caldera has been conducted over three, colinear paths: 46 km to the Pohakuloa saddle between Mauna Kea and Mauna Loa, 207 km to Kahului, Maui and 465 km to the ACO situated on the sea floor 114 km north of Oʻahu. The propagation path to Pohakuloa is shallow, 1990 m uphill from the mean earthquake depths. The path to Maui traverses to a depth ~7 km beneath the distal flanks of Mauna Kea, Mauna Loa, Hualālai, Kohala and Haleakelā. The path to ACO continues beneath the distal flanks of Pu`u Kukui and Wailau and then ~263 km beneath the sea floor (>3000 m bathymetric depth). A fourth segment estimates the attenuation between Maui and ACO by separating out the shared Kīlauea–Maui contribution. The Pohakuloa segment is compared with prior attenuation studies of the Island of Hawaiʻi. The traverse to Maui is new. The 70 per cent oceanic traverse from Maui to ACO is compared with a prior attenuation study in the oceanic lithosphere near Wake Island.

The paths within the volcanos (to POHA and KHLH) show both significant similarities as well as differences. Both show Q_P and Q_S initially increasing with frequency from ~100 near 1.5 Hz. Both show Q_S increasing with frequency below 1.5 Hz (resolution is limited by bandwidth) to 300–400. Both show significant bulk attenuation. The principle difference is the frequency quasi-independence of Q_P and Q_S (in the range 400–600) above ~10 Hz observed for the shallow, short propagation to POHA. For KHLH, both $\frac{\mathrm{d}Q_P}{\mathrm{d}f}$ and $\frac{\mathrm{d}Q_S}{\mathrm{d}f}$ have similar trends of ~33 Hz^{-1}, whereas for POHA the $\frac{\mathrm{d}Q_P}{\mathrm{d}f}$ and $\frac{\mathrm{d}Q_S}{\mathrm{d}f}$ trends (>10 Hz) differ in sign. Also, Q_S over the path to KHLH may be fit reasonably well by a Debye relaxation peak, whereas at POHA the fit is poor.

Low values of frequency-independent $Q < 100$ observed within the shallow (<3 km) summit of Kīlauea in prior studies (Fig. 4) are not observed over the 46 km path to Pohakuloa. However, the Q_S derived from Q-coda by Chouet (1976) offer the best fit to the POHA Q_S data, expressing both an initial increasing Q (<10 Hz) and then flattening over the band 9–24 Hz.

For the path to ALOHA, $Q_S > Q_P > Q_K$ over all frequencies. Over the paths to KHLH and to ALOHA, roughly identical linear trends are observed for Q_P and for Q_K. However, Q_S shows a more rapid linear increase for ALOHA than KHLH, indicating that the oceanic segment from KHLH to ALOHA has significantly higher Q_S. By deriving the Q's for the KHLH$\longrightarrow$ALOHA segment of propagation, an oceanic path contribution is resolved. For this KHLH$\longrightarrow$ALOHA segment, Q_S increases linearly, more rapidly with frequency, $\frac{\mathrm{d}Q_S}{\mathrm{d}f} \cong 138$, than other paths. In contrast, the $\frac{\mathrm{d}Q_P}{\mathrm{d}f} \sim 30$ is concordant with that seen for the KHLH and ALOHA paths. Notwithstanding the moderately more attenuation, the Q_S values for this oceanic segment from Maui to ACO agree remarkably well with the attenuation study of Butler *et al.* (1987) near Wake Island. However, both the Q_P and Q_K are higher at Wake Island, indicating greater bulk attenuation for Hawaiian paths.

An apparent scattering Q for the Kīlauea to POHA path is derived from the fluctuating Q_S and Q_P values with respect to the attenuation trend line. By assuming a frequency independent $Q \sim 650 - 700$ concordant with the upper range of error bars for $f > 10$ Hz, the apparent losses above this threshold are mapped into $Q_{scattering} > 1000$. Here the intrinsic losses exceed the scattering losses, that is $Q_{scattering} > Q_{P\ and\ S}$, as observed in Hawaiʻi by Chouet (1976) and Mayeda *et al.* (1992)

In summary comparison, the following points are salient. (1) the path from Kīlauea to POHA shows multiple attenuation processes, Q_μ, Q_K, $Q_{scattering}$, $Q \sim f$ and Q ~constant; (2) for the paths to KHLH and ALOHA, the attenuation processes include Q_μ, Q_K and $Q \sim f$; (3) for the derived ocean segment KHLH$\longrightarrow$ALOHA, again Q_μ, Q_K, $Q \sim f$ are observed with Q_μ increasing rapidly with frequency compared to other paths and (4) in comparison with prior high-frequency attenuation measurements in the oceanic crust and lithosphere near Wake Island, Q_μ are comparable, and Q_P and Q_K are lower for the Hawaiian Islands.

In addition to the measurement of attenuation, I have attempted to resolve some constraints upon the attenuation process. Based upon the significant contrast in physical properties, I have proposed that bulk attenuation may be due to the conjunction of water saturated vesicles within basalt causing differential heating within the water and basalt matrix due the temperatures varying thermodynamically with imposed pressure variations from the seismic waves. Assuming the same attenuation process, using the ratio of Q_μ from the shallow POHA and deep KHLH paths, the molar volume $\bar{V}$, and temperature extrapolated from Hawaiʻi boreholes, an activation energy $E^* = 50$ kJ mol^{-1} is derived. Finally, the attenuation characteristics for shear losses in Q_S^{-1} may be matched to a single Debye peak in the attenuation spectrum at $f \sim 1.4$ Hz for the KHLH path.

11 CONCLUSION

I have measured effective anelastic attenuation from 50 M_w 5 earthquakes during the collapse of Kīlauea's caldera in 2018 over shallow and mid-crustal depths beneath Hawaiian volcanos, and extending into the oceanic crust at the ACO north of Oahu. Energy loss is measured with respect to an ω^{-2} earthquake source spectrum at three sites along a constant azimuth: IU.POHA Pohakuloa, at the saddle between Mauna Loa and Mauna Kea; PT.KHLH Kahului, Maui between Haleakalā and west Maui; and on the seafloor at ALOHA, ACO. Over the observed propagation paths, intrinsic attenuation losses exceed scattering losses, that is $Q_{scattering} > Q_{P\ and\ S}$. In general, compressional wave losses are greater than those for shear waves, and the additional loss is modelled as due to bulk attenuation losses via the modulus of incompressibility, *K*. I have further proposed that bulk loss mechanism is due to the contrasting physical properties between vesicular basalts and the water-saturated vesicles.

The paths to POHA and KHLH both exhibit similar Q increasing with frequency from 1 to 10 Hz. However, for POHA above 10 Hz, Q remains relatively constant to nearly 40 Hz. Apparent fluctuations in Q with respect to a constant trend are modelled as an additional loss due to elastic scattering, with apparent $Q > 1000$. Hence, in addition to bulk attenuation and apparent scattering Q, the 46-km shallow path to POHA exhibits both frequency independent and nearly constant Q trends.

The path to ALOHA has similar compressional and bulk losses as KHLH, but the effective shear losses appear much larger for KHLH. By using the Q spectrum for the Kīlauea–Kahului path segment, I have corrected the Kīlauea–Kahului–ACO path, to resolve the effective Q over a 70 per cent oceanic Kahului–ACO path. The effective, frequency-dependent Q_S measured increases from 600 to 1450 between 4 and 11 Hz. The rate of increase $\frac{\mathrm{d}Q_S}{\mathrm{d}f} \cong 138$ greatly exceeds other $\mathrm{d}Q/\mathrm{d}f$ trends in the range 20–45 Hz^{-1}. Comparing with a prior oceanic Q study near Wake Island (Butler *et al.* 1987) the results are congruent: evidence of bulk attenuation, and similar Q_S values and frequency dependence. However, both compressional and bulk losses are greater for the thicker oceanic crust between Kahului and ACO than observed in the Wake Island study.

Finally, I have modelled attenuation at KHLH as a Debye peak for a standard linear solid. Whereas the broad spectrum may be fit well, the smaller scale variations observed in Q^{-1} cannot be matched. This observation spurred the assumption of elastic scattering Q to describe the small-scale variation. By assuming the same attenuation mechanism in the frequency band 1.5–5.7 Hz for the shallow path to POHA and mid-crustal path to KHLH, I have derived an activation energy for the process.

DATA AND RESOURCES

All earthquake locations were obtained from the USGS/HVO catalogue (https://earthquake.usgs.gov/earthquakes/search/), and are listed in Table 1 of Butler (2018). Seismic waveform data for IU.POHA and PT.KHLH were downloaded from the IRIS Data Management System. ALOHA hydrophone data were downloaded from the University of Hawai‘i ACO.

ACKNOWLEDGEMENTS

I thank Don Thomas for discussions of Hawaiian boreholes, temperature gradients and thermal models for Hawai‘i. I thank Brian Shiro at the Hawaiian Volcano Observatory (HVO) for the velocity model used for locating Hawai‘i earthquakes. Cornelis Weemstra and an anonymous reviewer offered useful suggestions for the manuscript. I thank the Global Seismographic Network (NSF and USGS) and the NOAA Pacific Tsunami Warning Center for their operations of IU.POHA and PT.KHLH, respectively. I thank the University of Hawai‘i and the NSF for supporting the ACO. SOEST contribution number 11001. HIGP contribution number 2415.

REFERENCES

Aki, K., 1980. Scattering and attenuation of shear waves in the lithosphere, *J. geophys. Res.,* **85,** (B11), 6496–6504.

Aki, K. & Chouet, B., 1975. Origin of coda waves: source, attenuation, and scattering effects, *J. geophys.Res. ,* **85,** (23), 3322–3342.

Anderson, D.L., 1967. The anelasticity of the mantle, *Geophys. J. Int.,* **14**(1-4), 135–163.

Anderson, D.L., 1975. Chemical plumes in the mantle, *Bull. geol. Soc. Am.,* **86**(11), 1593–1600.

Anderson, D.L., 1980. Bulk attenuation in the Earth and viscosity of the core, *Nature,* **285**(5762), 204.

Anderson, D.L., 1989. *Theory of the Earth*. Blackwell Scientific Publications, p. 300.

Anderson, D.L. & Given, J.W., 1982. Absorption band Q model for the Earth, *J. geophys. Res.,* **87**(B5), 3893–3904.

Anderson, D.L. & Natland, J.H., 2005. A brief history of the plume hypothesis and its competitors: concept and controversy, *Spec. Pap.-Geol. Soc. Am.,* **388,** 119.

Batzle, M.L., Kumar, G., Hofmann, R., Duranti, L. & Adam, L., 2014. Seismic-frequency loss mechanisms: direct observation, *Leading Edge,* **33**(6), 656–662.

Brune, J.N., 1970. Tectonic stress and the spectra of seismic shear waves from earthquakes, *J. geophys. Res.,* **75**(26), 4997–5009.

Budiansky, B. & O'Connell, R.J., 1980. Bulk dissipation in heterogeneous media, in *Solid Earth Geophysics and Geotechnology,* pp. 1–10, ed. Nasser, S. N., American Society of Mechanical Engineers.

Butler, R., 1987. A seismic absorption band in the western Pacific lithosphere, *Bull. seism. Soc. Am.,* **77,** 266–269.

Butler, R., 2003. The Hawaii-2 Observatory: observation of nanoearthquakes, *Seism. Res. Lett.,* **74,** 290–297.

Butler, R., 2018. High-frequency (>100 Hz) earthquakes North of Moloka‘i detected on the seafloor at the Aloha cabled observatory high-frequency earthquakes North of Moloka‘i detected on the seafloor, *Bull. seism. Soc. Am.,* **108**(5A), 2739–2747.

Butler, R., 2019. Composite earthquake source mechanism for 2018 M w 5.2–5.4 Swarm at Kīlauea Caldera: antipodal source constraint, *Seismol. Res. Lett.,* **90**(2A), 633–641.

Butler, R., 2020. Volcanic earthquake foreshocks during the 2018 collapse of Kīlauea Caldera, *Geophys. J. Int.,* **220**(1), 71–78.

Butler, R. & Duennebier, E.K., 2000. Observations of high-frequency Po and So phases propagating in the Northeastern Pacific lithosphere at the Hawaii-2 Observatory, *EOS, Trans. Am. geophys. Un. Supp.,* **81,** F837.

Butler, R., McCreery, C.S., Frazer, L.N. & Walker, D.A., 1987. High-frequency seismic attenuation of oceanic P- and S-waves in the western Pacific, *J. geophys. Res.,* **92,** 1383–1396.

Butler, R. *et al.*, 2000. Hawaii-2 observatory pioneers opportunities for remote instrumentation in ocean studies, *EOS, Trans. Am. Geophys. Un.,* **81**(15), 157–163.

Butler, R. *et al.*, 2004. The Global Seismographic Network surpasses its design goal, *EOS, Trans. Am. Geophys. Un.,* **85**(23), 225–232.

Carcolé, E. & Sato, H. 2010. Spatial distribution of scattering loss and intrinsic absorption of short-period S waves in the lithosphere of Japan on the basis of the Multiple Lapse Time Window Analysis of Hi-net data, *Geophys. J. Int.,* **180**(1), 268–290.

Castellan, G.W. 1964. *Physical Chemistry*. Addison-Wesley, pp. 717.

Chouet, B., 1976, Source, scattering and attenuation effects on high frequency seismic waves, *Doctoral dissertation,* Massachusetts Institute of Technology.

Cormier, V.F., 1982. The effect of attenuation on seismic body waves, *Bull. seism. Soc. Am.,* **72**(6B), S169–S200.

Dahlen, F.A. & Tromp, J., 1998. *Theoretical Global Seismology,* Princeton Univ. Press.

Davies, G.F., 1994. Thermomechanical erosion of the lithosphere by mantle plumes, *J. geophys. Res.,* **99**(B8), 15 709–15 722.

Durek, J.J. & Ekstro¨m, G., 1996. A radial model of anelasticity consistent with long-period surface-wave attenuation, *Bull. seism. Soc. Am.,* **86**(1A), 144–158.

Dziewonski, A.M. & Anderson, D.L., 1981. Preliminary reference Earth model, *Phys. Earth planet. Inter.,* **25**(4), 297–356.

Eulenfeld, T. & Wegler, U. 2017. Crustal intrinsic and scattering attenuation of high-frequency shear waves in the contiguous United States, *J. geophys. Res.,* **122**(6), 4676–4690.

Frankel, A. & Wennerberg, L., 1987. Energy-flux model of seismic coda: separation of scattering and intrinsic attenuation, *Bull. seism. Soc. Am.,* **77**(4), 1223–1251.

Garcia, M.O., Haskins, E.H., Stolper, E.M. & Baker, M., 2007. Stratigraphy of the Hawai ‘i Scientific Drilling Project core (HSDP2): Anatomy of a Hawaiian shield volcano, *Geochemistry, Geophysics, Geosystems,* **8**(2), 37 pp.

Goetze, C., 1978. The mechanisms of creep in olivine, *Phil. Trans. R. Soc. Lond., A,* **288**(1350), 99–119.

Hanks, T.C. & Thatcher, W., 1972. A graphical representation of seismic source parameters, *J. geophys. Res.,* **77**(23), 4393–4405.

Hansen, S., Thurber, C., Mandernach, M., Haslinger, F. & Doran, C., 2004. Seismic velocity and attenuation structure of the east rift zone and south flank of Kilauea Volcano, Hawaii, *Bull. seism. Soc. Am.,* **94**(4), 1430–1440.

Jackson, D.D. & Anderson, D.L., 1970. Physical mechanisms of seismic-wave attenuation, *Rev. Geophys.,* **8**(1), 1–63.

Jackson, I. & Faul, U.H., 2010. Grainsize-sensitive viscoelastic relaxation in olivine: Towards a robust laboratory-based model for seismological application, *Physics of the Earth and Planetary Interiors,* **183**(1-2), 151–163.

Jerram, D.A., Millett, J.M., Kück, J., Thomas, D., Planke, S., Haskins, E., Lautze, N. & Pierdominici, S., 2019. Understanding volcanic facies in the subsurface: a combined core, wireline logging and image log data set from the PTA2 and KMA1 boreholes, Big Island, Hawaii, *Scient. Drilling,* **25,** 15–33.

Kaneko, Y. & Shearer, P.M., 2014. Seismic source spectra and estimated stress drop derived from cohesive-zone models of circular subshear rupture, *Geophys. J. Int.,* **197**(2), 1002–1015.

, eds Kasahara, J., Stephen, R.A., Kasahara, J., Stephen, R.A., Acton, G.D. & Frey, F.A, 2006. Leg 200 synthesis: a broadband seismic station in oceanic crust at the Hawaii-2 Observatory and coring into the Nuuanu Landslide, in *Proc. ODP, Sci. Results,* pp. 200.

Kennett, B.L.N., Furumura, T. & Zhao, Y., 2014. High-frequency P_o/S_o guided waves in the oceanic lithosphere: II—heterogeneity and attenuation, *Geophys. J. Int.,* **199**(1), 614–630.

Klein, F.W., Frankel, A.D., Mueller, C.S., Wesson, R.L. & Okubo, P.G., 2001. Seismic hazard in Hawaii: high rate of large earthquakes and probabilistic ground-motion maps, *Bull. seism. Soc. Am.,* **91**(3), 479–498.

Knopoff, L., 1964. Q, *Rev. Geophys.,* **2,** 625–660.

Kohlstedt, D.L., Goetze, C. & Durham, W.B., 1976. Experimental deformation of single crystal olivine with application to flow in the mantle, in *The Physics and Chemistry of Minerals and Rocks,* pp. 35–49,ed. Runcorn, S., Wiley.

Koyanagi, S., Aki, K., Biswas, N. & Mayeda, K., 1995. Inferred attenuation from site effect-corrected *T* phases recorded on the island of Hawaii, *pure and applied geophysics,* **144**(1), 1–7.

Larson, R.L., Fisher, A.T., Jarrard, R.D., Becker, K., Leg, O.D.P. & Party, S.S., 1993. Highly permeable and layered Jurassic oceanic crust in the western Pacific, *Earth planet. Sci. Lett.,* **119**(1-2), 71–83.

Leahy, G.M., Collins, J.A., Wolfe, C.J., Laske, G. & Solomon, S.C., 2010. Underplating of the Hawaiian Swell: evidence from teleseismic receiver functions, *Geophys. J. Int.,* **183**(1), 313–329.

Lin, G., Shearer, P.M., Amelung, F. & Okubo, P.G., 2015. Seismic tomography of compressional wave attenuation structure for Kīlauea Volcano, Hawai'i, *J. geophys. Res.,* **120,** 2510–2524.

Mayeda, K., Koyanagi, S., Hoshiba, M., Aki, K. & Zeng, Y., 1992. A comparative study of scattering, intrinsic, and coda Q^{-1} for Hawaii, Long Valley, and central California between 1.5 and 15.0 Hz, *J. geophys. Res.,* **97**(B5), 6643–6659.

Minster, J.B., 1978a. Transient and impulse responses of a one-dimensional linearly attenuating medium. I. Analytical results, *Geophys. J. R. astr. Soc.,* **52,** 479–501.

Minster, J.B., 1978b. Transient and impulse responses of a one-dimensional linearly attenuating medium. II. A parametric study, *Geophys. J. R. astr. Soc.,* **52,** 503–524.

Morgan, W.J., 1971. Convection plumes in the lower mantle, *Nature,* **230**(5288), 42–43.

Morgan, W.J., 1972. Deep mantle convection plumes and plate motions, *AAPG Bull.,* **56**(2), 203–213.

Neal, C.A., *et al.*, 2019. The 2018 rift eruption and summit collapse of Kīlauea Volcano, *Science,* **363**(6425)367–374.

Park, J., Lindberg, C.R. & Vernon, F.L., 1987. Multitaper spectral analysis of high-frequency seismograms, *J. geophys. Res.,* **92**(B12), 12 675–12 684.

Romanowicz, B. & Durek, J.J., 2000. Seismological constraints on attenuation in the Earth: a review, *Am. Geophys. Un. Geophys. Monogr. Ser.,* **117,** 161–179.

Sato, H., Fehler, M.C. & Maeda, T., 2012, Seismic wave propagation and scattering in the heterogeneous Earth, in *Seismic Wave Propagation and Scattering in the Heterogeneous Earth,* 2nd edn, Springer Berlin Heidelberg. doi:10.1007/978-3-642-23029-5_2.

Scherbaum, F. & Wyss, M., 1990. Distribution of attenuation in the Kaoiki, Hawaii, source volume estimated by inversion of P wave spectra, *J. geophys. Res.,* **95**(B8), 12 439–12 448.

Shearer, P.M., Prieto, G.A. & Hauksson, E., 2006. Comprehensive analysis of earthquake source spectra in southern California, *J. geophys. Res.,* **111**(B6), doi:10.1029/2005JB003979.

Shito , A,, Suetsugu, D., Furumura, T., Sugioka , H. & Ito, A., 2013. Small-scale heterogeneities in the oceanic lithosphere inferred from guided waves, *Geophys. Res. Lett.,* **40,** 1708–1712.

Slagle, A.L. & Goldberg, D.S., 2011. Evaluation of ocean crustal Sites 1256 and 504 for long-term CO2 sequestration, *Geophysical research letters,* **38**(16), L16307.

Stolper, E.M., DePaolo, D.J. & Thomas, D.M., 2009. Deep drilling into a mantle plume volcano: the Hawaii Scientific Drilling Project, *Scient. Drilling,* **7,** 4–14.

Takahashi, T., 2012. Three-dimensional attenuation structure of intrinsic absorption and wide-angle scattering of S waves in northeastern Japan, *Geophys. J. Int.,* **189**(3), 1667–1680.

Takemura, S., Kobayashi, M. & Yoshimoto, K., 2017. High-frequency seismic wave propagation within the heterogeneous crust: effects of seismic scattering and intrinsic attenuation on ground motion modelling, *Geophys. J. Int.,* **210**(3), 1806–1822.

Takeuchi, N., Kawakatsu, H., Shiobara, H., Isse, T., Sugioka, H., Ito, A. & Utada, H., 2017. Determination of intrinsic attenuation in the oceanic lithosphere-asthenosphere system, *Science,* **358**(6370), 1593–1596.

Thomas, D.M., Lienert, B.R. & Wallin, E., 2015. Three-dimensional magnetotelluric modeling of the Pohukuloa training area, Hawaii Island, in *AGU Fall Meeting Abstracts,* GP13A.

van IJsseldijk, J., Ruigrok, E., Verdel, A. & Weemstra, C., 2019. Shallow crustal imaging using distant, high-magnitude earthquakes, *Geophys. J. Int.,* **219**(2), 1082–1091.

Volcanoes of the National Parks of Hawai'i, 2006. Available at: https://www.nps.gov/parkhistory/online_books/hawaii-notes/vol4-2-7d.htm.

Walker, D.A. & McCreery, C.S., 1987. Po/So phases, *J. Phys. Earth,* **35**(2), 111–125.

Walker, G.P., 1989. Spongy pahoehoe in Hawaii: a study of vesicle-distribution patterns in basalt and their significance, *Bull. Volcanol.,* **51**(3), 199–209.

Watts, A.B. & Ten Brink, U.S., 1989. Crustal structure, flexure, and subsidence history of the Hawaiian Islands, *J. geophys. Res.,* **94**(B8), 10 473–10 500.

Wei, S.S. & Wiens, D.A., 2020. High bulk and shear attenuation due to partial melt in the Tonga-Lau back-arc mantle, *J. geophys. Res.,* **125**(1), doi:10.1029/2019JB017527.

Widmer, R., Masters, G. & Gilbert, F., 1991. Spherically symmetric attenuation within the Earth from normal mode data, *Geophys. J. Int.,* **104**(3), 541–553.

Wilson, J.T., 1963. A possible origin of the Hawaiian Islands, *Can. J. Phys.,* **41**(6), 863–870.